

AD-A112 464 WESTERN RESEARCH CORP SAN DIEGO CA
DESIGN SUPPORT OF A RARE GAS HALIDE LASER. (U)
MAR 82 R SCHERS
WRC-R-310

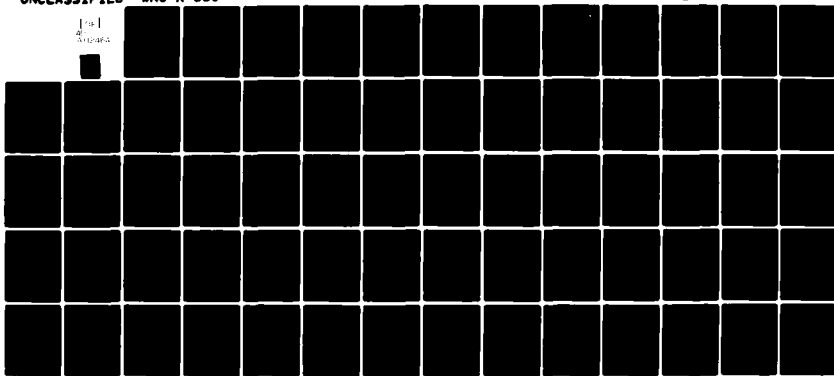
F/6 20/5

N00173-80-C-0226

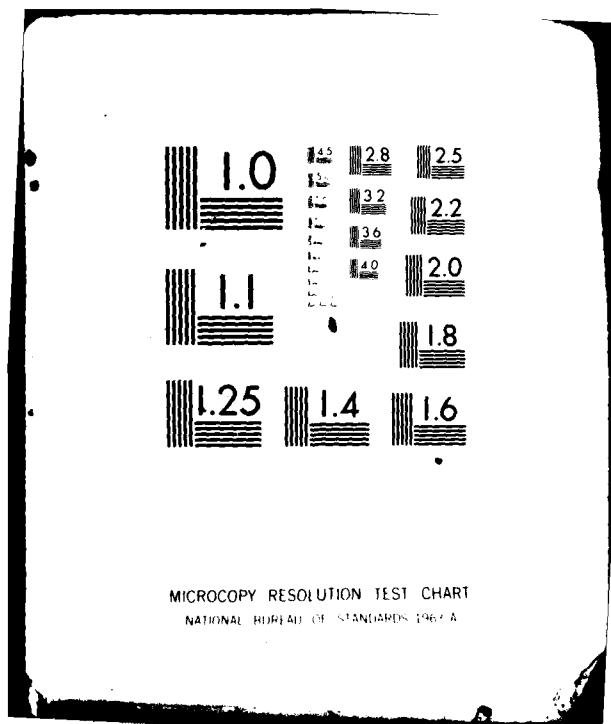
ML

UNCLASSIFIED

101
R
310A



END
DATE
TIME
4-82
RTIC



12

WRC-R-310

ADA112464

FINAL TECHNICAL REPORT:
DESIGN SUPPORT OF A RARE GAS HALIDE LASER

Prepared For: OFFICE OF NAVAL RESEARCH
Physics Program Office
Arlington, VA 22217

Contract No.: N00173-80-C-0226

Period of Performance: 23 June 1980 -- 8 October 1980

1

Distribution Statement : Approved for public release;
distribution unlimited

Prepared By: Richard Scheps
WESTERN RESEARCH CORPORATION
8616 Commerce Avenue
San Diego, California 92121

Reproduction in whole or in part is permitted for
any purpose of the United States Government

3 March 1982

82 03 24 070

DTIC
MAR 23 1982

ST

UNCLASSIFIED

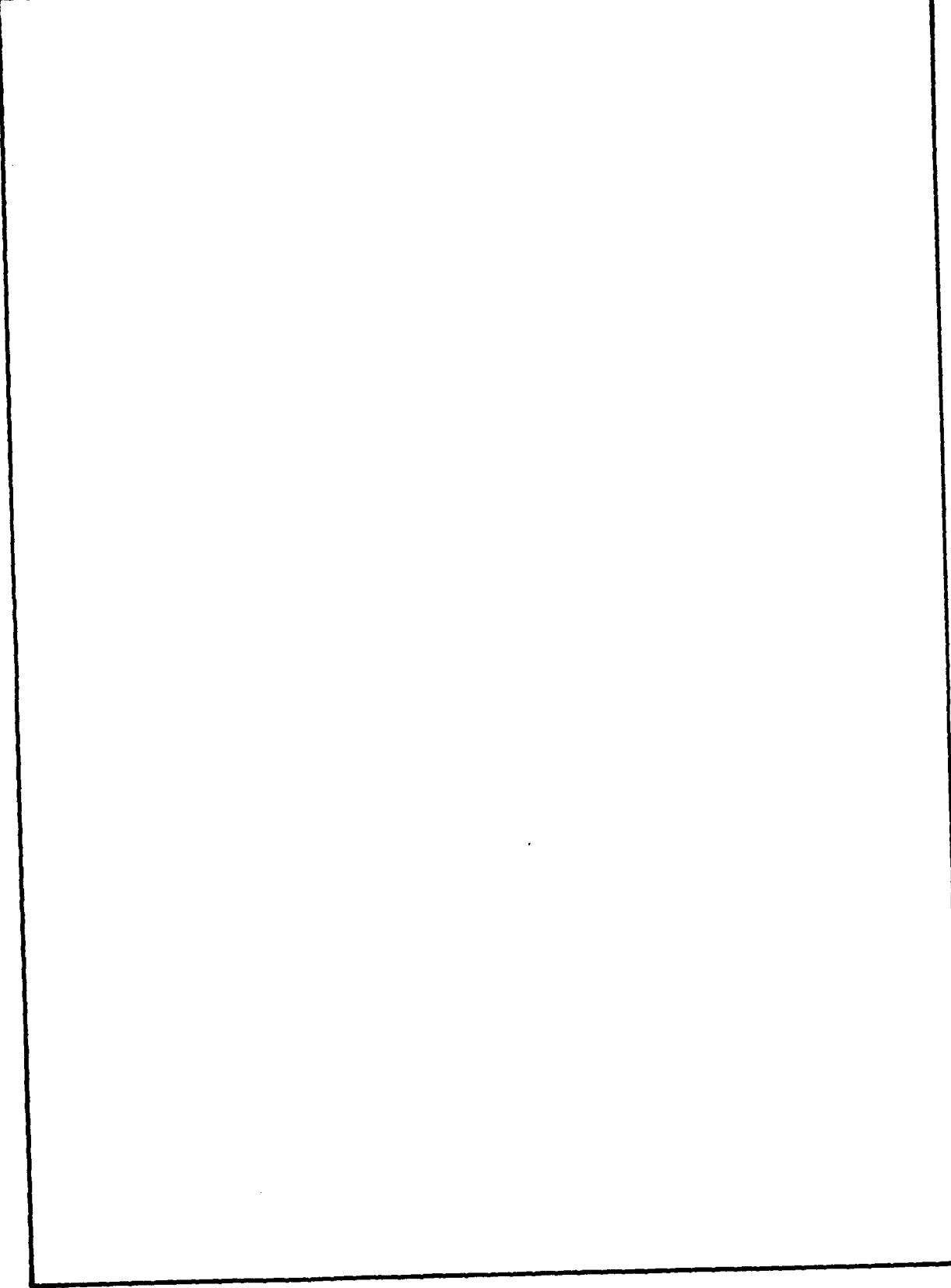
SECURITY CLASSIFICATION OF THIS PAGE (When Data Entered)

DD FORM 1 JAN 73 1473 EDITION OF 1 NOV 68 IS OBSOLETE
S/N 0102- LF: D14-6601

Unclassified

SECURITY CLASSIFICATION OF THIS PAGE (When Data Enforced)

UNCLASSIFIED
SECURITY CLASSIFICATION OF THIS PAGE (When Data Entered)



S/N 0102-LF-014-6601

Unclassified
SECURITY CLASSIFICATION OF THIS PAGE (When Data Entered)

WRC-R-310

FINAL TECHNICAL REPORT:
DESIGN SUPPORT OF A RARE GAS HALIDE LASER

Prepared For: OFFICE OF NAVAL RESEARCH
Physics Program Office
Arlington, VA 22217

Contract No.: N00173-80-C-0226

Period Of
Performance: 23 June 1980 - 8 October 1980

Distribution
Statement : Approved for public release;
distribution unlimited

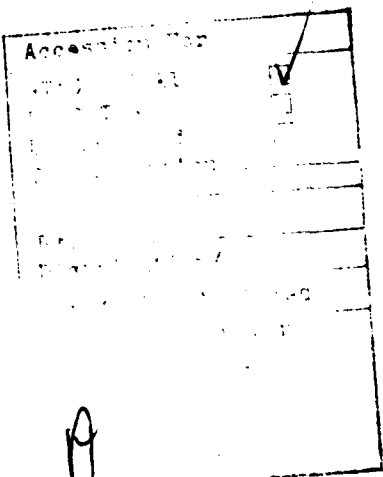
Prepared By: Richard Scheps
WESTERN RESEARCH CORPORATION
8616 Commerce Avenue
San Diego, California 92121

Reproduction in whole or in part is permitted for
any purpose of the United States Government

3 March 1982

TABLE OF CONTENTS

	<u>Page</u>
INTRODUCTION	5
TYPICAL DESIGN	6
OUTPUT ENERGY AND UNIFORMITY	6
ELECTRICAL DESIGN CONSIDERATIONS	19
Electron Energy Deposition	19
Diode Dynamics	20
Electrical Driver Design	46
Summary and Recommendations for Electrical Design	59
OPTICS AND MOUNTS	61
OTHER SUBSYSTEMS	65
COST SUMMARY	66



DESIGN SUPPORT OF A RARE GAS HALIDE LASER FOR THE NAVAL RESEARCH LABORATORY

INTRODUCTION

In support of construction of a large XeCl device by the Naval Research Laboratory, a design and cost analysis has been prepared by Western Research Corporation. Rare gas halide lasers have reached the point where fairly large systems may be designed with some confidence. The success of a particular laser design depends on the ability to combine knowledge acquired in experimental work on small scale and scaling experiments, with an understanding of the technologies involved, such as electron beams and large optics. In this report, we summarize the results of the WRC program in which the practical design of a large system is described and analyzed.

The statement of work consists of a design analysis, cost analysis and specification formulation. This report discusses these aspects in the context of output and energy uniformity, electrical driver design, energy deposition and electrical performance, and system cost. The specific system considered is the NRL generated design using two opposing e-beams pumping a 40 cm x 30 cm by 2 meter volume. The foil separation is 40 cm. The gas mixture is 4 atm of Ne/Xe/HCl with Xe and HCl representing 1% and 0.067% of the mixture, respectively. The saturation flux is 5×10^5 W/cm², and a pulse length of 10^{-6} s is assumed.

TYPICAL DESIGN

The design of the device hinges on a knowledge of the performance of the active medium as coupled to the optical field. Once the chamber geometry, pressure, and energy are set, the various subsystems may be specified. A typical design component layout is shown in Figure 1.

For the proposed design a 10^{-6} s pulse length is assumed, and a beam voltage of 0.42 megavolts is required, based on previous experience. An average current density of 10 A/cm^2 is transmitted through a 2 mil titanium foil, depositing 24 kilojoules per side with an applied magnetic field of 1.25 kilogauss. The output beam spatial uniformity design point of ± 0.30 is expected to be attained.

Among the critical design considerations, the energy output depends primarily upon relatively uniform injection of the electron beam pump source, the spatial and temporal dependence of the kinetic parameters, and the optical system chosen. The temporal history of gain and absorption, the output window coatings for damage threshold, the optical design tolerance for changes in pump and kinetic parameters during the pulse, and the transfer efficiency from stored energy to injected beam energy all directly affect the output energy and must be considered in the final design. The guide field, beam energy and foil separation mentioned above are designed to give good beam quality at the required output energy.

OUTPUT ENERGY AND UNIFORMITY

Laser beam irradiance uniformity is a major factor in determining the design suitability of the present laser. The output energy and efficiency of conversion are controlled by small volume performance and standard length scaling arguments. The assumed 10^{-6} s pulse length and 10 A/cm^2

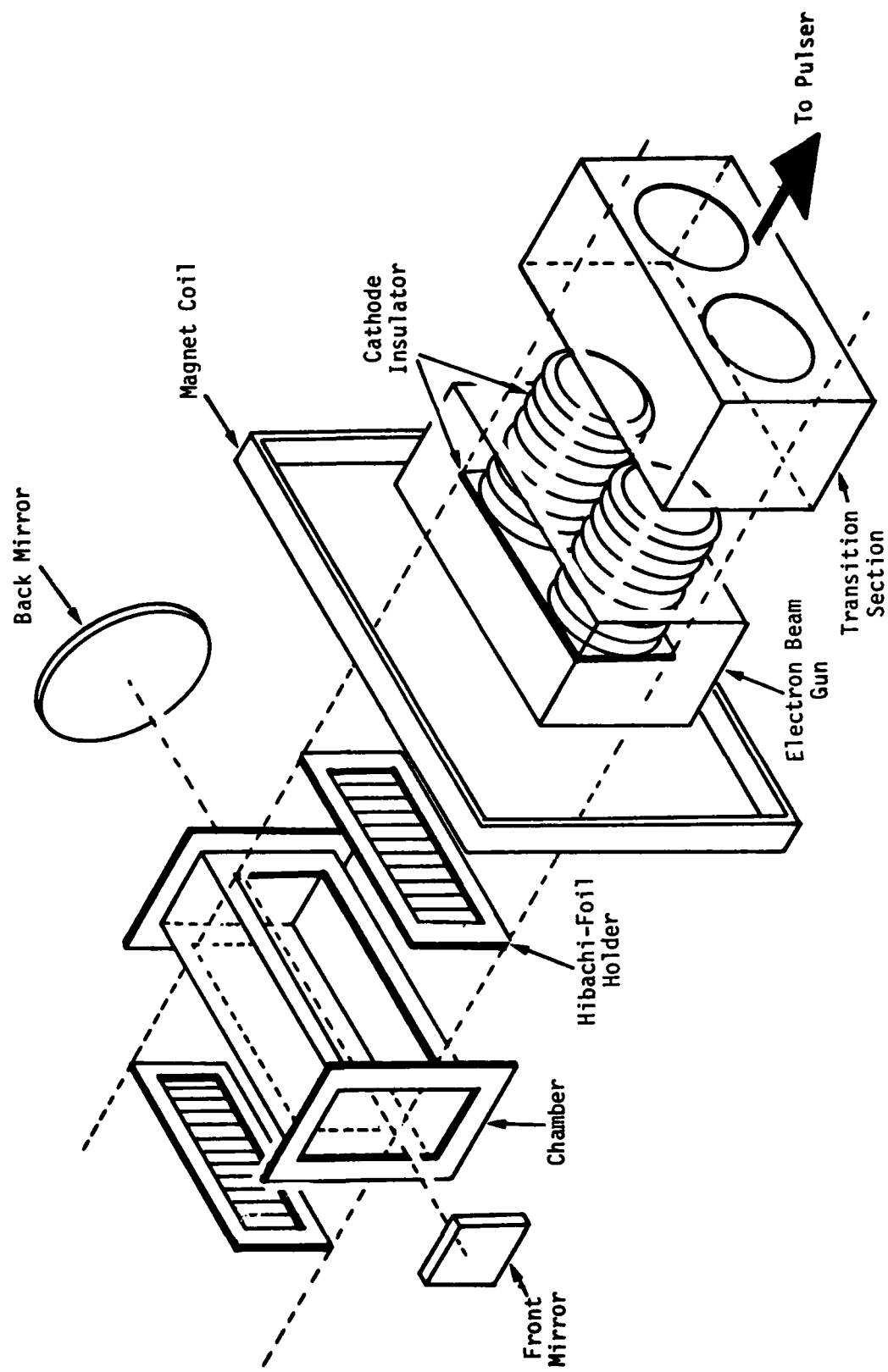


Figure 1. Laser system components.

transmitted current lead to 10 joules per liter out at 5% local efficiency. The energy deposited in the gas is 48 kilojoules and is related to the current density j and beam voltage V_b by

$$E_n = jV_b A \tau_p$$

where A is the foil area and τ_p is the pulse length. The total volume is 250 liters, giving a volumetric energy deposition of 200 joules/liter. A local efficiency of 5% results in 10 joules/liter out. Gains in the system under these conditions will be between 2% and 3% per cm. This performance is in excess of that thought to be desired. However, for the 0.5 MW/cm^2 saturation flux and gain to absorption of 10, the efficiency could be only $\sim 3\%$. A 500 nsec pulse length has severe implications as to the cost and performance of the electrical drivers.

The temporal behavior of the absorption and gain will determine how well the fixed cavity extracts energy. This latter effect depends on the detailed kinetics, an area in which NRL is well versed. As far as tradeoffs in the resonator design are concerned, the unstable resonator is less efficient in extraction but the extraction efficiency is less sensitive to absorption changes. Stable resonators, on the other hand, are more efficient in extraction, and can be shown to be more sensitive to absorption changes.

The spatial and temporal uniformity depend primarily upon the pump uniformity and upon the uniformity of the kinetic rates involved in the saturation flux and absorption.

For a uniformly pumped laser oscillator with no macroscopic density or index gradients, the output irradiance homogeneity is determined by the spatial and temporal dependence of the extraction efficiency.

Variations in the kinetics resulting from temperature increases due to energy deposition and halogen burnup will determine the temporal dependence of the quenching rates and hence the temporal dependence of the extraction efficiency in the e-beam pumped XeCl laser. Nonuniform E-fields created by return currents in the uniformly pumped medium will affect the electron capture rate and hence establish an electron density gradient across the aperture. In cases where electron quenching is an important process, as it might well be in XeCl, the extraction efficiency will become spatially coupled to the local E-fields. The phase shift due to the electron density gradient can be calculated from the plasma dispersion relation and is negligible.

For the homogeneously broadened XeCl laser, we can adapt Rigrod's analysis to write for the extraction efficiency

$$\eta = \frac{\beta_0}{g_0 L} \left(\frac{1-r_2}{\sqrt{r_2}} \right) \left(\frac{R-A}{R+Q} \right) \quad (1)$$

where η = extraction efficiency

$$\beta_0 = \sqrt{\beta_+ \beta_-}$$

$\beta_{+,-}$ = irradiance in the $+z$ or $-z$ direction, relative to the saturation irradiance

r_2 = the output mirror reflectivity ($r_1 = 1$)

R = lower level removal rate in XeCl

$A = 9 \times 10^7 \text{ sec}^{-1}$, Einstein A coefficient for XeCl

Q = total of all quenching rates

Note that the output irradiance β_{out} is

$$\beta_{\text{out}} = \beta_0 \left(\frac{1-r_2}{\sqrt{r_2}} \right) . \quad (2)$$

Rigrod's treatment of the flux transport equations results in the approximation

$$\beta_{\text{out}} = \frac{(g_0 - \alpha_0) L + \ln \sqrt{r_2}}{1 - \frac{\alpha_0 L}{\ln \sqrt{r_2}}} \quad (3)$$

where g_0 is the unsaturated gain coefficient, α_0 is the absorption coefficient, and L is the cavity length. The approximate solution proposed by Rigrod is in excellent agreement with the more exact treatment of the flux transport, given by Schindler at Rocketdyne. We can write

$$\eta = \eta(Q, P, \alpha_0) \quad (4)$$

where the dependence of η on quenching and upper level pumping rates comes from the steady state solution to the two level homogeneously broadened laser, given by

$$g_0 = \left(\frac{R-A}{Q+A} \right) \frac{\sigma P}{R} . \quad (5)$$

P is the upper level population rate and σ is the stimulated emission cross section.

As the e-beam pulse progresses in time, gas kinetic heating will affect the quenching and upper level pump rates. Three body formation rates (including quenching) scale as $e^{W/T}$ where W is a characteristic energy in °K, while two body rates might be expected to scale with velocity i.e., with \sqrt{T} . This latter temperature dependence is observed for two body quenching in Kr_2F^* reported by NRL, and for electron capture by dissociative attachment to F_2 , observed by Trainor at AVCO. In addition, when electron loss is dominated by dissociative attachment to HCl, HCl burnup results in an increased electron density and increased electron quenching. Similarly, the dissociative attachment rate is spatially dependent on the local E-fields and this gives rise to a spatially dependent electron quenching rate. The absorption variations arise from several sources, including Xe_2Cl^* formation rate variations, and dimer ion and noble gas excimer removal rate variations.

The total variation in η is given by

$$d\eta = \frac{\partial \eta}{\partial Q} dQ + \frac{\partial \eta}{\partial \alpha_0} d\alpha_0 + \frac{\partial \eta}{\partial P} dP . \quad (6)$$

For small changes in the independent variables, Equation (6) can be linearized (Δ^2 and higher terms dropped) giving

$$\Delta\eta \approx \frac{\partial \eta}{\partial Q} \Delta Q + \frac{\partial \eta}{\partial \alpha_0} \Delta \alpha_0 + \frac{\partial \eta}{\partial P} \Delta P . \quad (7)$$

The fractional change in η can be obtained from Equations (1)-(7). This is

$$\begin{aligned}
 \frac{\Delta\eta}{\eta} = & \left(\frac{Q(R-A)}{(Q+A)(Q+R)} - \frac{g_o L}{(g_o - \alpha_o)L + \ln\sqrt{r_2}} \frac{Q}{Q+A} \right) \frac{\Delta Q}{Q} \\
 & + \left[\frac{\gamma}{\left(\frac{\ln\sqrt{r_2}}{\alpha_o L} - 1 \right) \left(\frac{\ln\sqrt{r_2}}{\alpha_o L} + (\gamma-1) \right)} \right] \frac{\Delta \alpha_o}{\alpha_o} \\
 & + \left(\frac{\alpha_o L - \ln\sqrt{r_2}}{\ln\sqrt{r_2} + (g_o - \alpha_o)L} \right) \frac{\Delta P}{P} \quad (8)
 \end{aligned}$$

where $\gamma = g_o/\alpha_o$. We can analyze the present XeCl design case with $g_o L = 5$, $\alpha_o L = .5$, $\gamma = 10$, $r_2 = .11$ (optimum r_2 using Rigrod analysis), and using kinetic values of $Q = 10^8 \text{ sec}^{-1}$, $A = 9 \times 10^7 \text{ sec}^{-1}$, and $R = 9 \times 10^8 \text{ sec}^{-1}$.

Equation (8) then assumes the value

$$\frac{\Delta\eta}{\eta} = -.35 \frac{\Delta Q}{Q} -.40 \frac{\Delta \alpha_o}{\alpha_o} + .48 \frac{\Delta P}{P} \quad (9)$$

Any desired uniformity in $\Delta\eta/\eta$ must therefore be accompanied by a comparable uniformity in the spatial and temporal variation of Q , α_o and P . For example a 30% variation in P leads to a 15% variation in η .

The output irradiance is the primary design parameter, and we can write

$$\begin{aligned}
 \frac{\Delta\beta_{\text{out}}}{\beta_{\text{out}}} &= \left(\frac{Q}{Q+A} \right) \left(\frac{-g_o L}{(g_o - \alpha_o) L + \ln \sqrt{r_2}} \right) \left(\frac{\Delta Q}{Q} \right) \\
 &+ \frac{\gamma}{\left(\frac{\ln \sqrt{r_2}}{\alpha_o L} - 1 \right) \left(\frac{\ln \sqrt{r_2}}{\alpha_o L} + (\gamma-1) \right)} \left(\frac{\Delta \alpha_o}{\alpha_o} \right) \\
 &+ \frac{g_o L}{(g_o - \alpha_o) L + \ln \sqrt{r_2}} \frac{\Delta P}{P} . \quad (10)
 \end{aligned}$$

For the design point, this equation is equal to

$$\frac{\Delta\beta_{\text{out}}}{\beta_{\text{out}}} = - .77 \frac{\Delta Q}{Q} - .40 \frac{\Delta \alpha_o}{\alpha_o} + 1.5 \frac{\Delta P}{P} . \quad (11)$$

Thus the output uniformity is substantially more sensitive to the pump rate and quenching rate variations than the extraction efficiency.

In XeCl the kinetic rate variations are not well characterized as a function of temperature and E/N. It is therefore useful to treat the problem parametrically. The mirror reflectivity is optimized for a set $g_o L$ and $\alpha_o L$, and as the medium kinetics change, the output coupling remains fixed and hence laser operation proceeds in a non-optimized cavity. This non-optimum behavior is quite different from the optimized extraction efficiency dependence on g_o and α_o (which is treated by Rigrod).

Figure 2 shows $g_0 L$ plotted as a function of η for $\alpha_0 L$ values ranging between .1 and 1. These curves are obtained from the exact solution of the Rigrod analysis, since Schindler shows Rigrod's approximation to be in error for $g_0 L \gtrsim 10$. The infinite gain limit for each curve is given by α_0 and the reflectivity. Figure 3 shows curves of constant extraction efficiency in $\alpha_0 L$, $g_0 L$ space, where each η is indexed to the extraction efficiency at the design point, which in this case is $\eta = .46$ at $r_2 = .11$. Both $g_0 L$ and $\alpha_0 L$ change independently during the pulse, and the effect of this change can be determined by plotting the trajectory of $\alpha_0 L$, $g_0 L$ points on Figure 3 with the design point as the origin. (Figure 3 was obtained in the same manner as Figure 2 i.e., using the exact solution to Rigrod's flux transport equation.)

An increase in $\alpha_0 L$ at fixed $g_0 L$ would be represented by a horizontal line in Figure 3. An increase in $\alpha_0 L$ of 20% leads to a decrease in η of $\sim 10\%$. This is also predicted in Equation (9). A vertical line represents changing $g_0 L$ at fixed $\alpha_0 L$, while $\alpha_0 L$ and $g_0 L$ changing at fixed γ is represented by a 45° line in the figure.

Several features of Figure 1 are worth noting. First, the worst of all trajectories arises from decreasing $g_0 L$ and increasing $\alpha_0 L$ equal fractional amounts. Large reductions in $g_0 L$ ($>25\%$) are almost as bad, with $\Delta\eta/\eta \sim \Delta g_0 L/g_0 L$ at fixed α_0 . Large increases in $g_0 L$ at fixed $\alpha_0 L$ tend to "saturate" out at $\sim 30\%$. This results from the fact that as $g_0 L \rightarrow \infty$ η limits out, as shown in Figure 2. Physically, at high $g_0 L$ the optimum extraction efficiency approaches 1 but r_2 is fixed at the original design point. The output therefore does not increase as fast as $g_0 L$ due to the finite absorption and non-zero reflectivity. Finally, note that the case where $g_0 L$ increases and $\alpha_0 L$ decreases is only slightly better than the worst case ($g_0 L$ decreases, $\alpha_0 L$ increases).

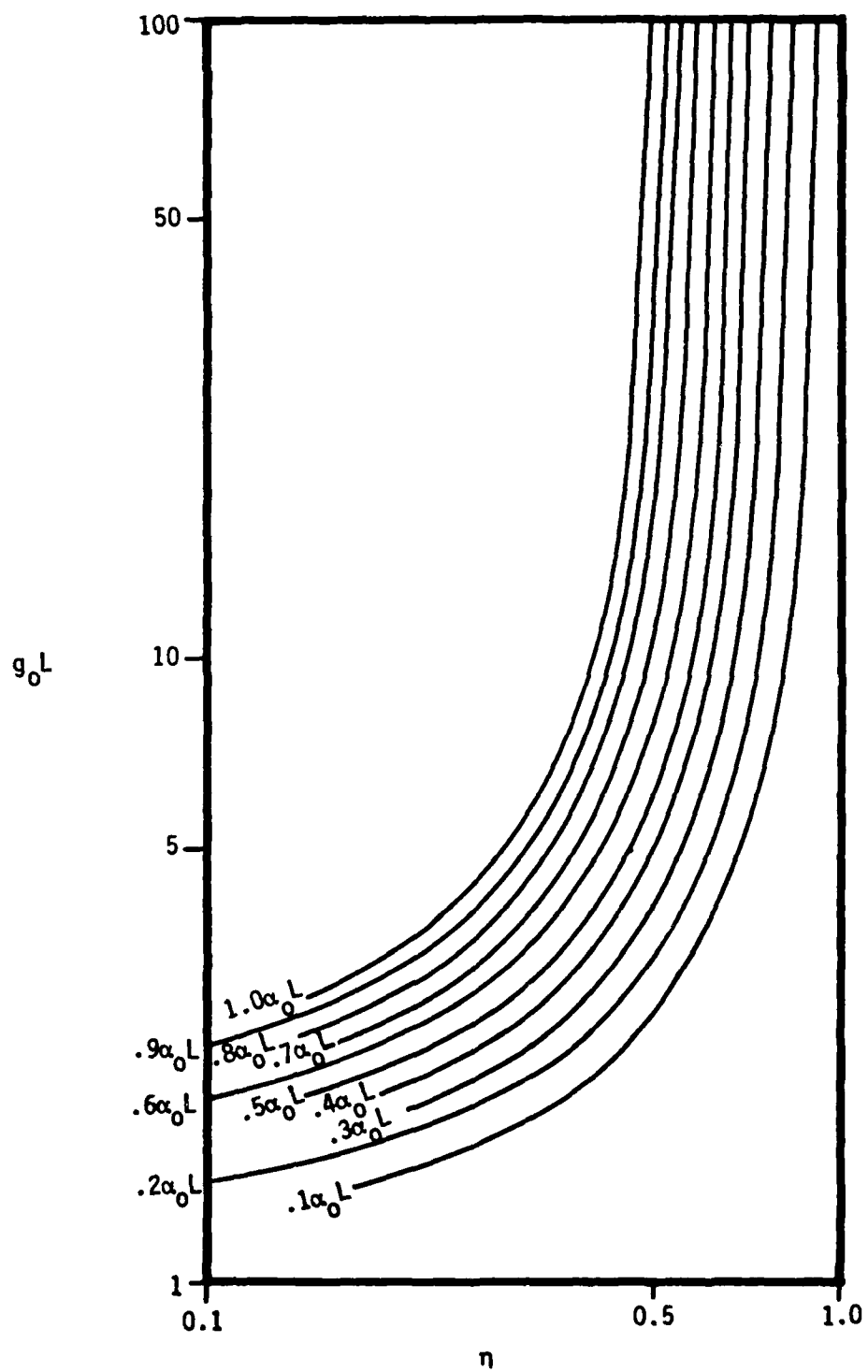


Figure 2. $g_0 L$ plotted as a function of η for values of $\alpha_0 L$ ranging between 0.1 and 1.

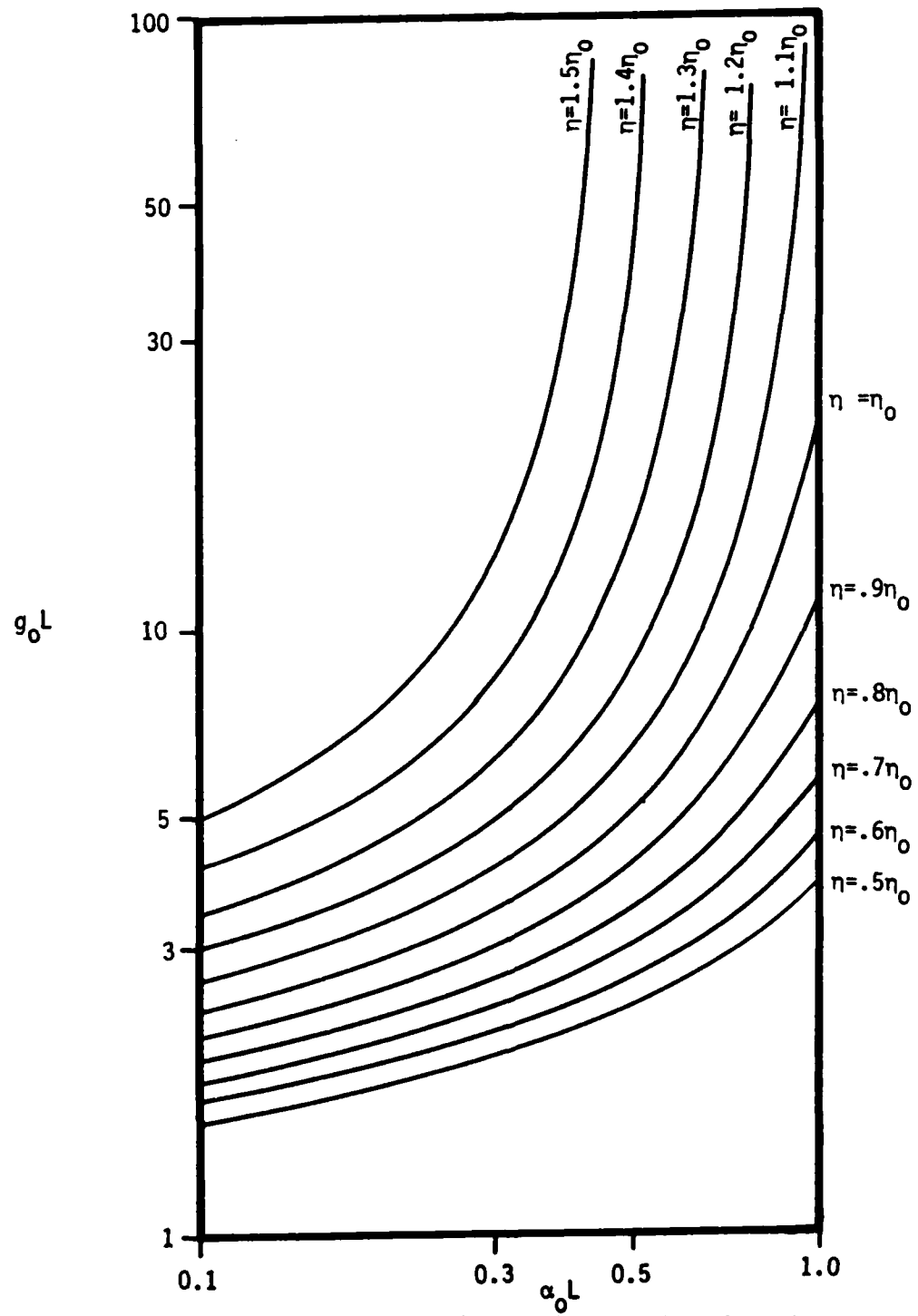


Figure 3. Curves of constant extraction efficiency in $\alpha_0 L$, $g_0 L$ space, where each η is indexed to the extraction at the design point, which in this case is $\eta = 0.46$ at $r_2 = 0.11$.

Clearly the most desirable case arises where $g_o L$ and $\alpha_o L$ change in the proportion given by the constant η curves in Figure 3. However, the trajectory of $g_o L / \alpha_o L = \text{constant}$ is also desirable. An 80% increase in both $g_o L$ and $\alpha_o L$ result in only a 10% increase in η , while 40% decreases in these same parameters result in a 10% decrease in η .

Note that with the exception of the design point in Figure 3, all η are below the optimum η since the cavity reflectivity will be too high or too low for any other pair of gain and absorption values. Therefore changes in η with $g_o L$ and $\alpha_o L$ generally will be different in sign and/or magnitude than the corresponding changes in the optimum η . For example, the point $g_o L = 2, \alpha_o L = .1$ is on the $\eta = .8 \eta_o$ curve, representing a 20% decrease in the design point extraction efficiency of .46. However, the optimum extraction efficiency at $g_o L = 2, \alpha_o L = .1$ is $\eta = .60$, representing a 30% increase in η .

Curves similar to those shown in Figure 3 may be constructed for any design point. The case of $g_o L = 6, \alpha_o L = .6$ is shown in Figure 4, representing the 3 cm^{-1} gain, $\gamma = 10$, example. The consideration involved in optimizing the XeCl laser performance for irradiance uniformity and extraction efficiency (assuming uniform energy deposition) arises from selecting the design point in such a manner as to minimize the effects of anticipated $g_o L$ and $\alpha_o L$ changes without great sacrifices in the extraction efficiency. In some cases the preferred design point may be one which is never actually achieved in the particular laser device. Consider a laser cavity reflectivity optimized for $g_o L = 5, \alpha_o L = .5$ as in Figure 3, but with $g_o L = 10, \alpha_o L = 1$ at the onset of "steady state," changing to $g_o L = 20, \alpha_o L = 1$ at pulse termination. The curves show that the extraction efficiency will be below the $\eta = 1.1 \eta_o$ curve at pulse termination, and in both cases the extraction efficiency is $\eta \sim .9 \eta_{\text{opt}}$. However, if the cavity had been optimized for $g_o L = 10, \alpha_o L = 1$ and the final point were still $g_o L = 20$,

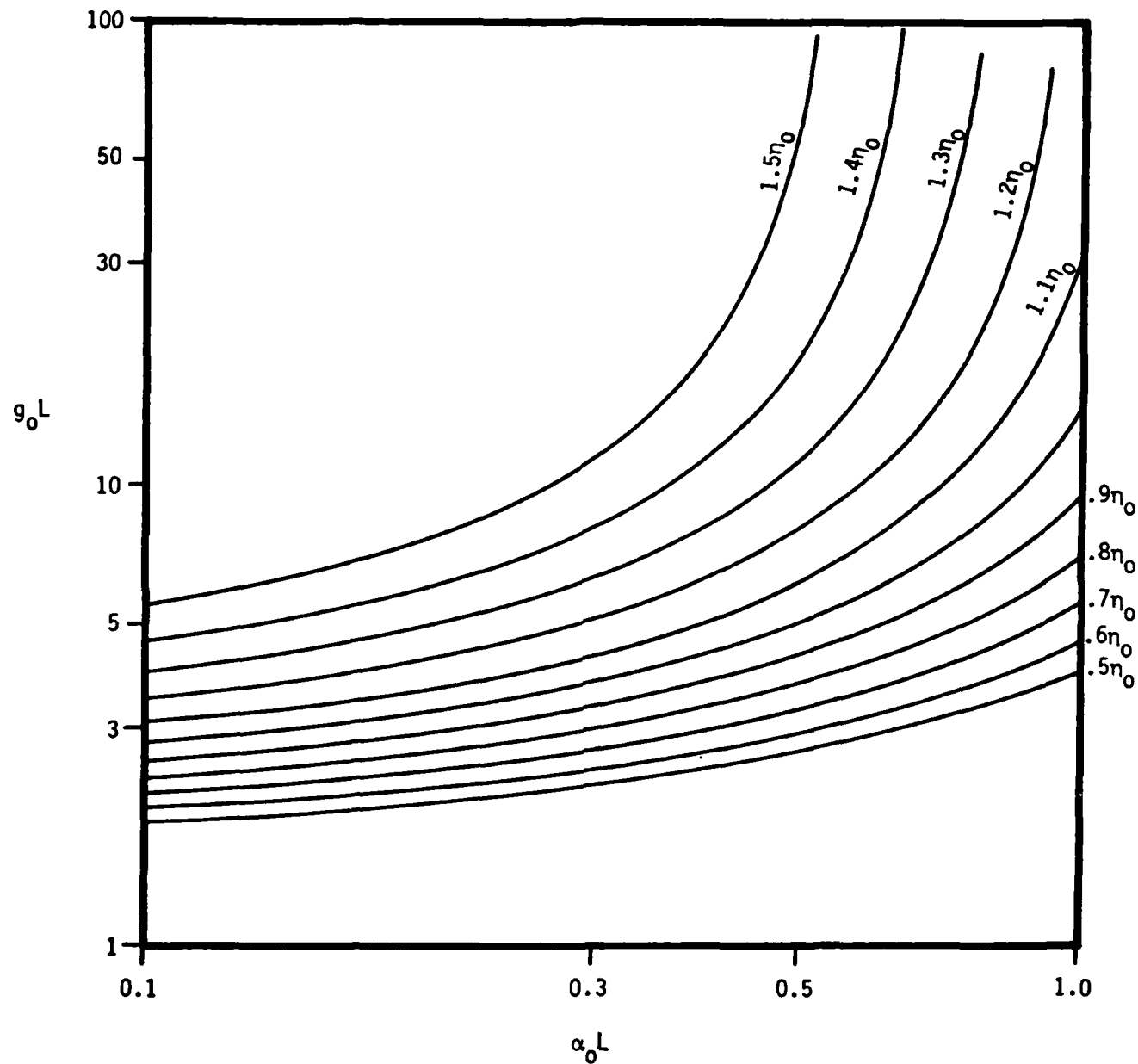


Figure 4. Curves of constant extraction efficiency for design point
 $g_0 = 6$, $\alpha_0 L = 0.6$.

$\alpha_0 L = 1$, the variation in η would be over 20%, i.e. the final point would be above the $\eta = 1.2 \eta_0$ curve. This is roughly the same variation one would obtain in Figure 3 if $g_0 L$ at the design point were to double with $\alpha_0 L$ fixed at 0.5.

In summary, then, the design point for the stable resonator configuration should be set based on the expectations for the $\alpha_0 L$, $g_0 L$ variations and consistent with extraction efficiency requirements. The present analysis is for a stable resonator configuration since the efficiencies are greater than the unstable resonators. The variations in exit flux due to variations in the saturation flux in the unstable resonators are substantially different and should be analyzed. This latter task requires a computer code and a greater effort than could be justified for the present work.

ELECTRICAL DESIGN CONSIDERATIONS

The single most important part of the laser design involves the several aspects of the electrical driver and deposition hardware. The electrical design dominates any consideration given to device reliability, as well as efficiency and uniformity considerations. The costs for pulses shorter than 1 microsecond become large and one must weigh the advantages of the shorter pulse against the rapidly increasing costs. The several topics that will be considered in the electrical design are energy deposition in the active volume, diode dynamics and performance, driver circuit design, the magnetic guide field, and voltage standoffs. We will conclude this section with a discussion of recommendations for an electrical system.

Electron Energy Deposition

The electron energy deposition uniformity is set by the pump uniformity. A magnetic guide field can be used to enhance deposition

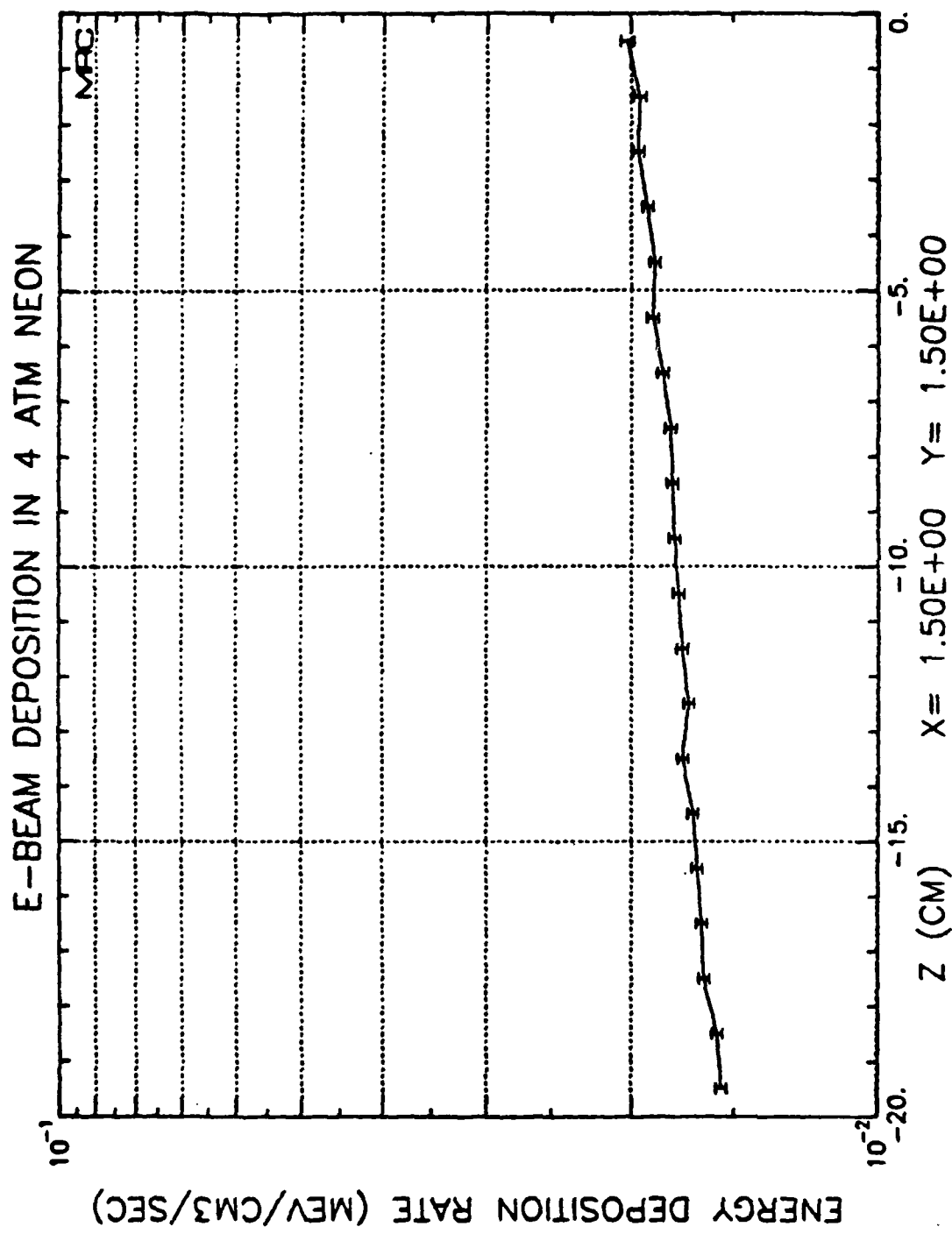
uniformity, and calculations of these effects can be made using Monte Carlo codes and analytical estimates. The overall deposition uniformity is coupled to the diode driver behavior. Previous studies for the Department of Energy indicated the impingement angle (transverse momentum) of the beam up to 20° will not seriously degrade beam uniformity. In addition, an edge gradient was found for a few centimeters at 2.5 kilogauss.

The electron beam, due to self fields, always has a finite perpendicular energy that is spatially correlated (usually near the edge). This leads to nonuniform deposition, as does the fact that the two opposing beams do not overlap uniformly in even the ideal case.

In the calculations for NRL, we find that uniformity within ± 0.13 can be maintained for voltage changes on the order of ± 0.10 in a 1 mil titanium foil, and voltage changes of ± 0.05 in a 2 mil foil. The results of analytical modelling of the energy deposition rate, particle flux, z component of current, and stopped particle accumulation, all as a function of the one-dimensional parameter z are given in Figures 5 - 28. These calculations are performed at a fixed x and y , and each set of curves represents a separate set of beam voltage and foil thickness conditions, as listed in Table 1. In addition, Table 1 summarizes the results of the calculations presented in Figures 5 - 28. These calculations are done for opposed beams with reflexing and using a titanium foil. Note that the plots show only half the deposition volume due to symmetry, and uniformity in Table 1 is defined as $2(E_{\max} - E_{\min})/(E_{\max} + E_{\min})$.

Diode Dynamics

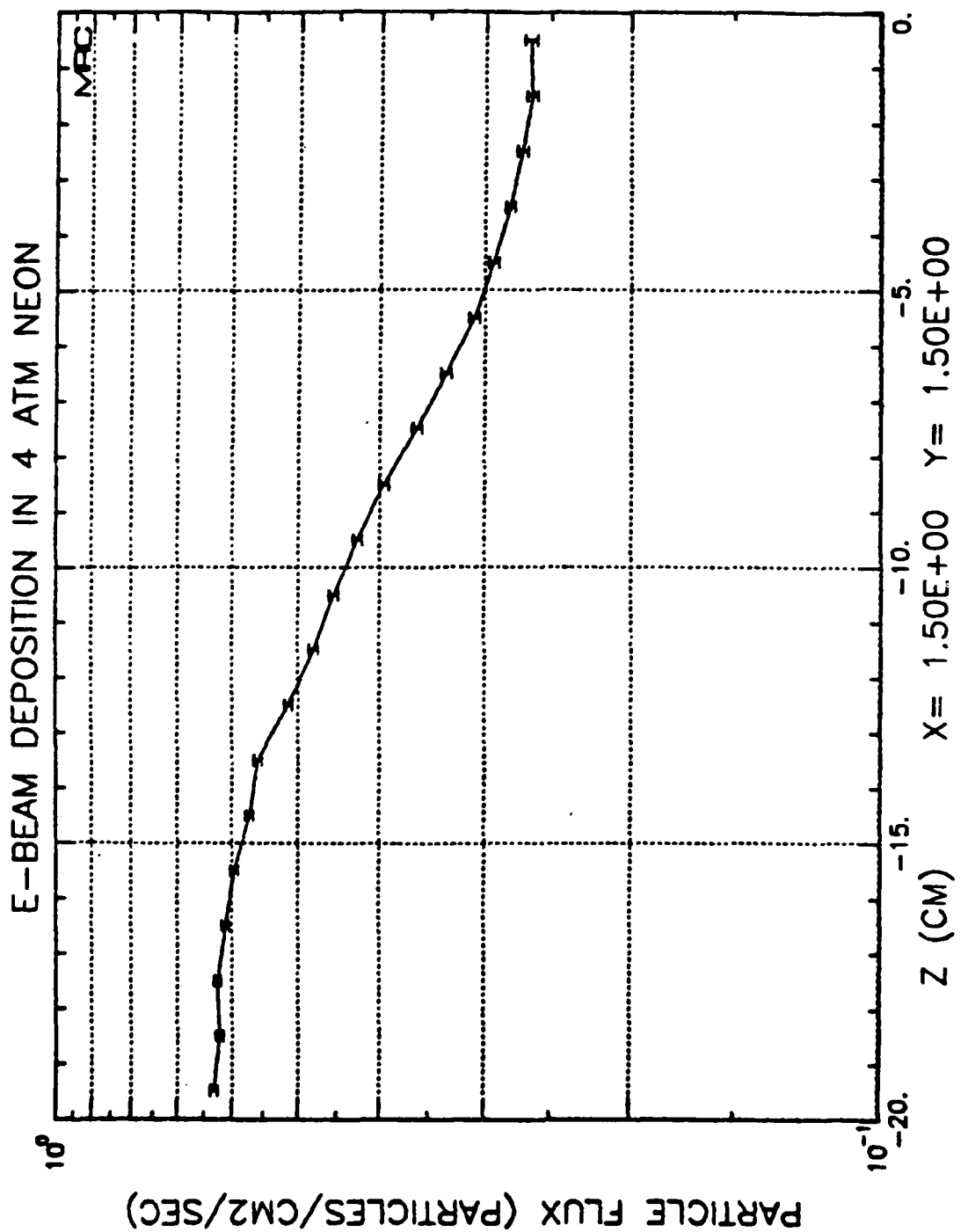
The diodes for this pulse length and uniformity are based on large area cold cathode emitters. The key to such cathodes is rapid and uniform ignition, particularly in a magnetic field. The B field affects electron flow by rotating the whole beam and shearing it at the ends. At fields of interest (~ 1 kilogauss), trajectories are near normal ($V_{\perp}/V_{\parallel} \approx 5^\circ$ at edge).

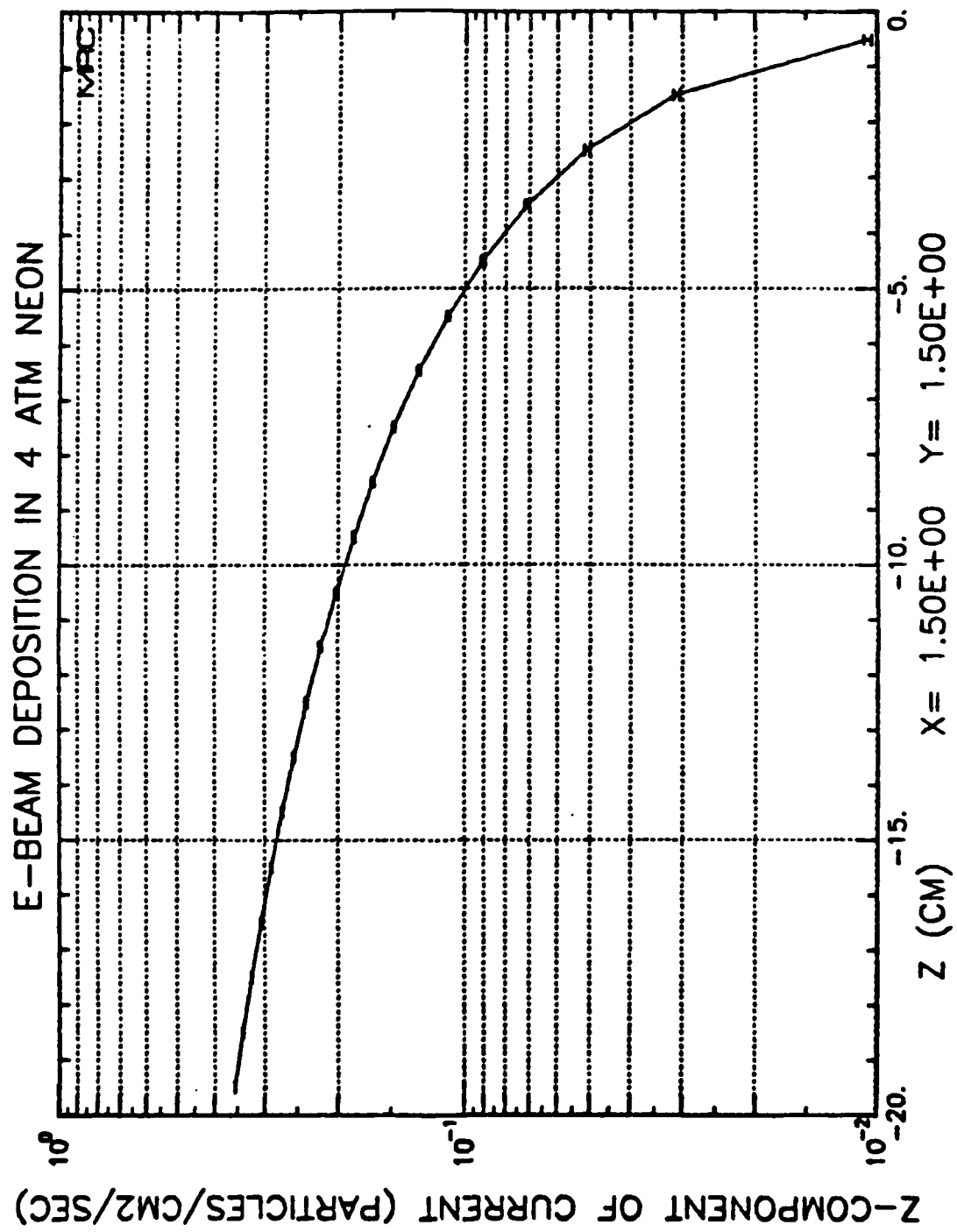


WRC-V-147

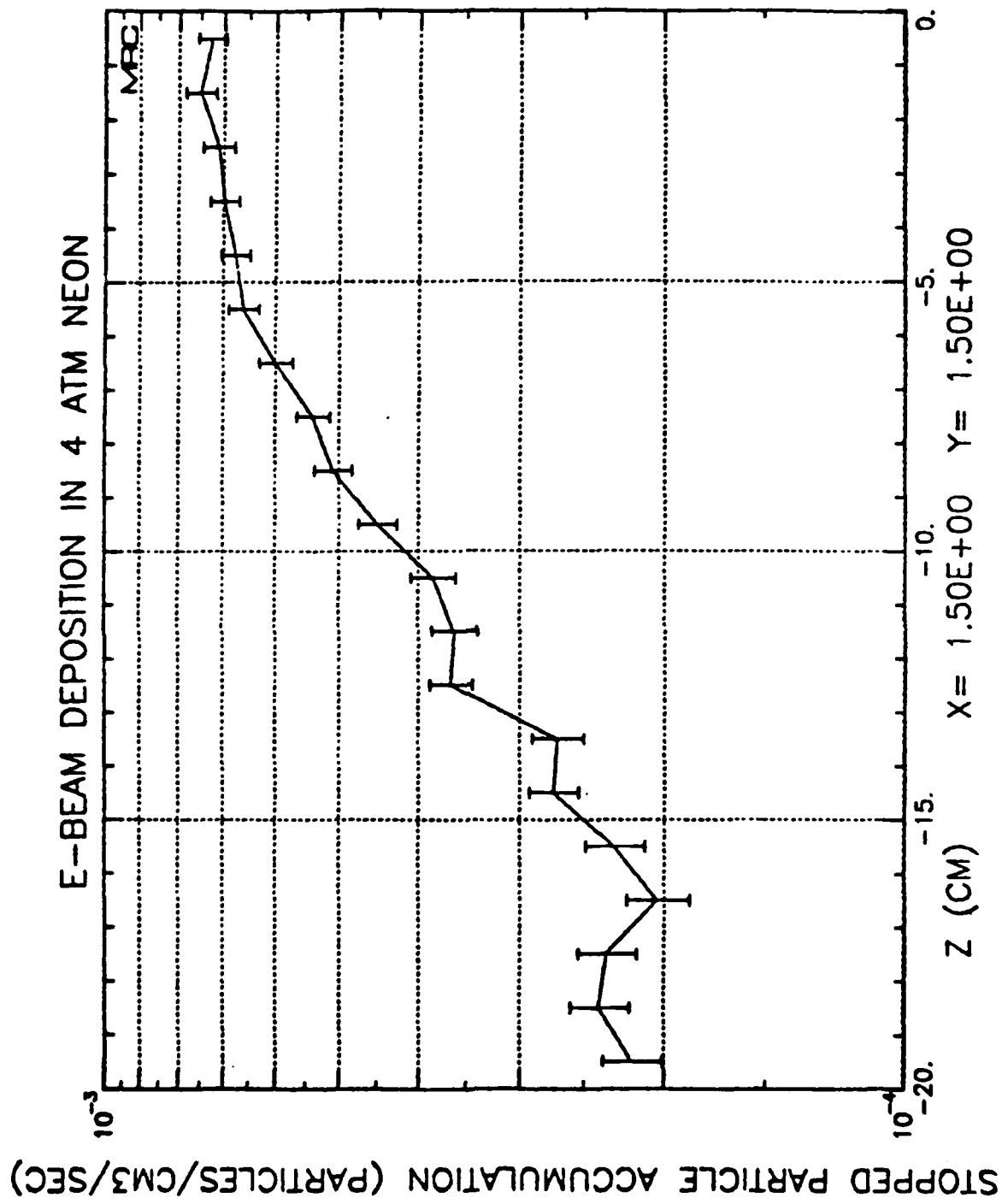
CASE NEON1MG 25-JUL-80 09:20:35

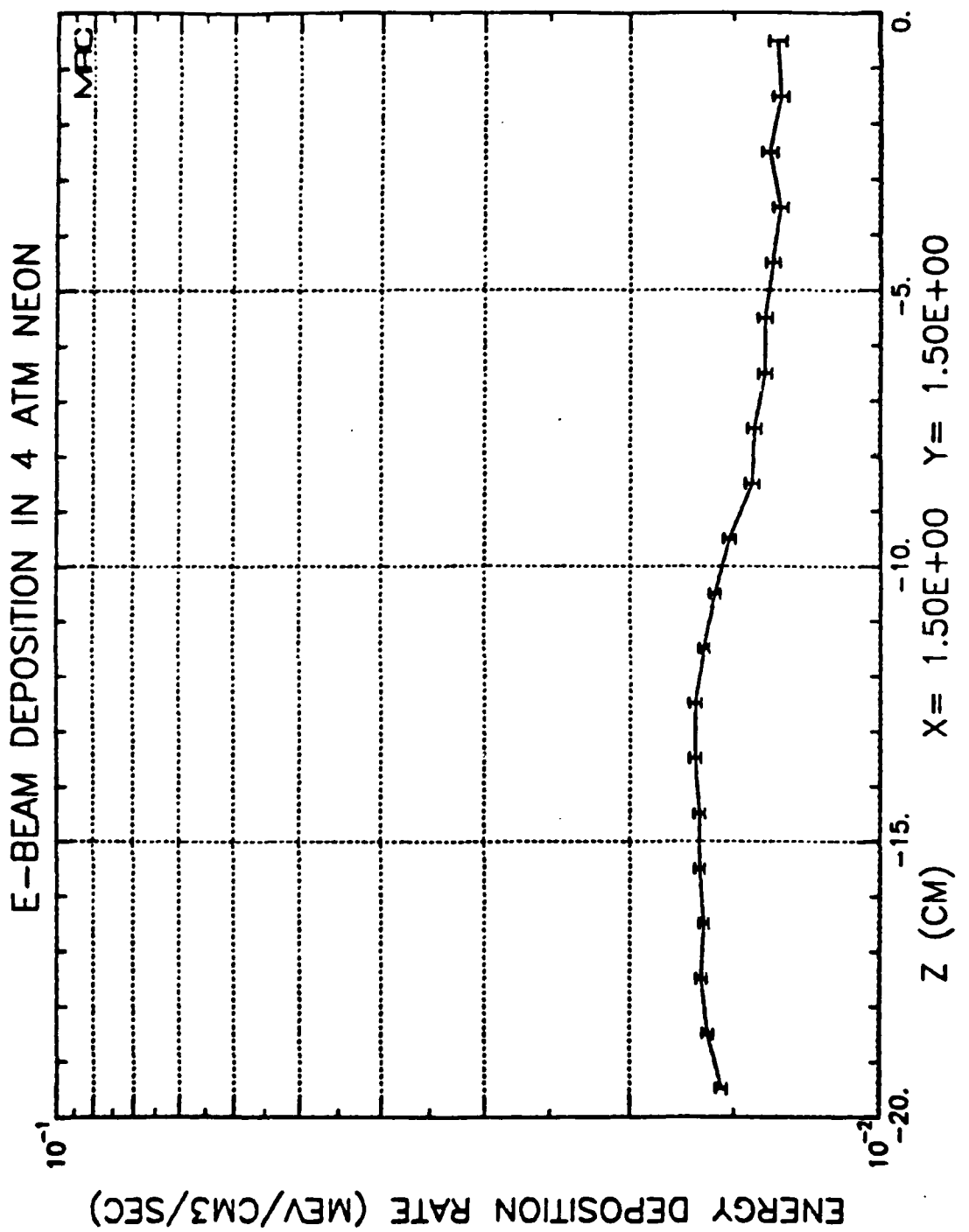
Figure 5.



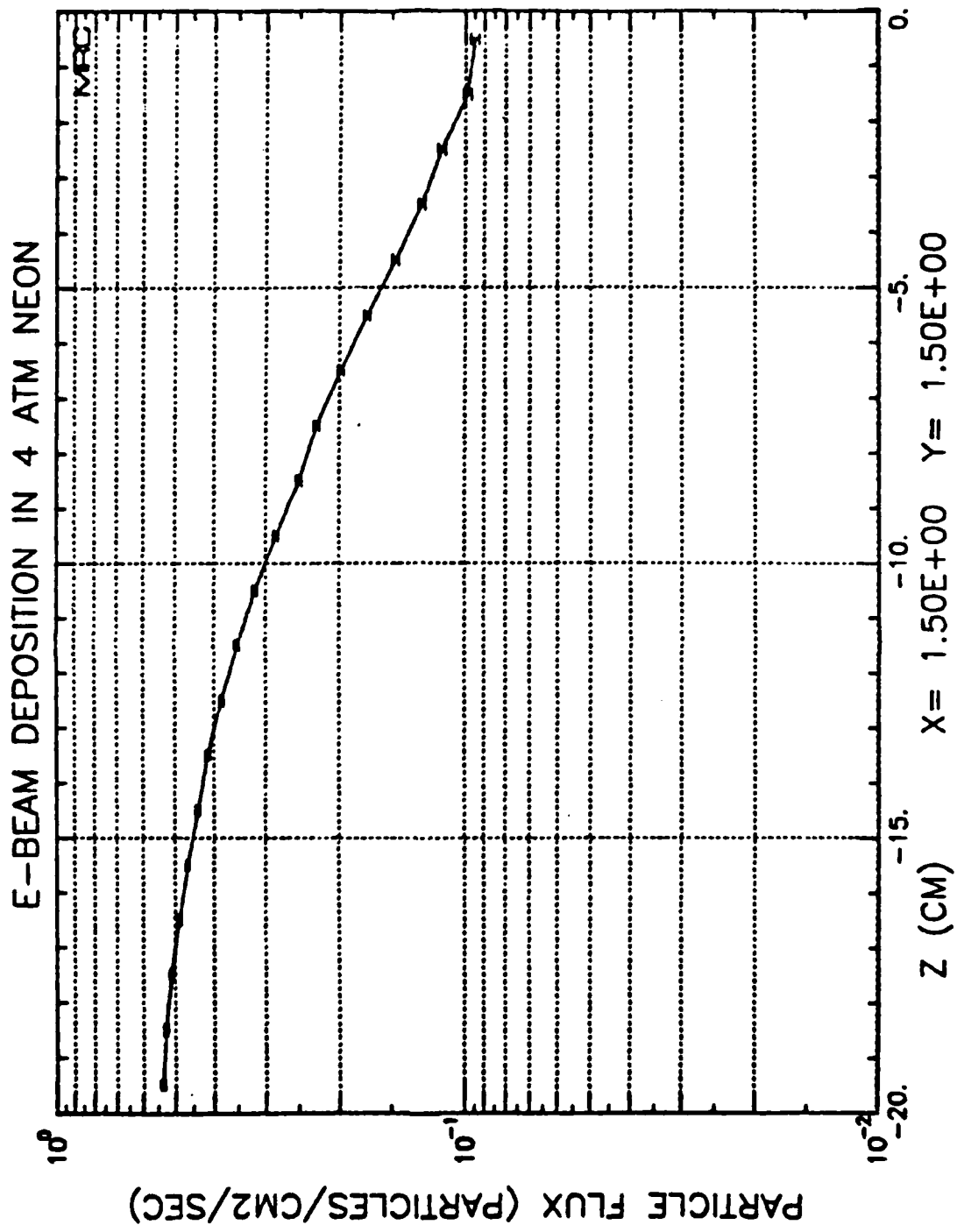


CASE NEON1M6 25-JUL-80 09:23:31
 Figure 7.

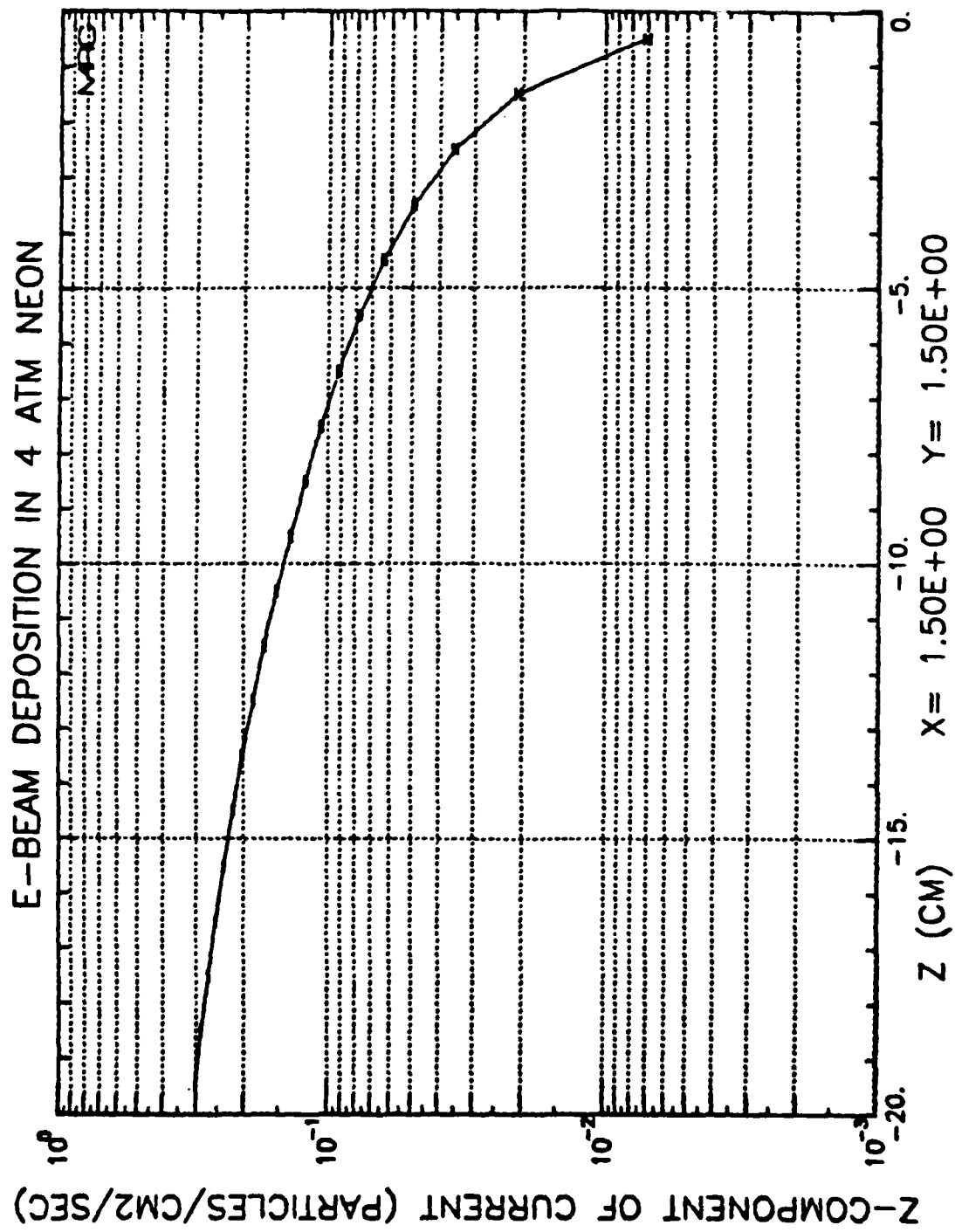




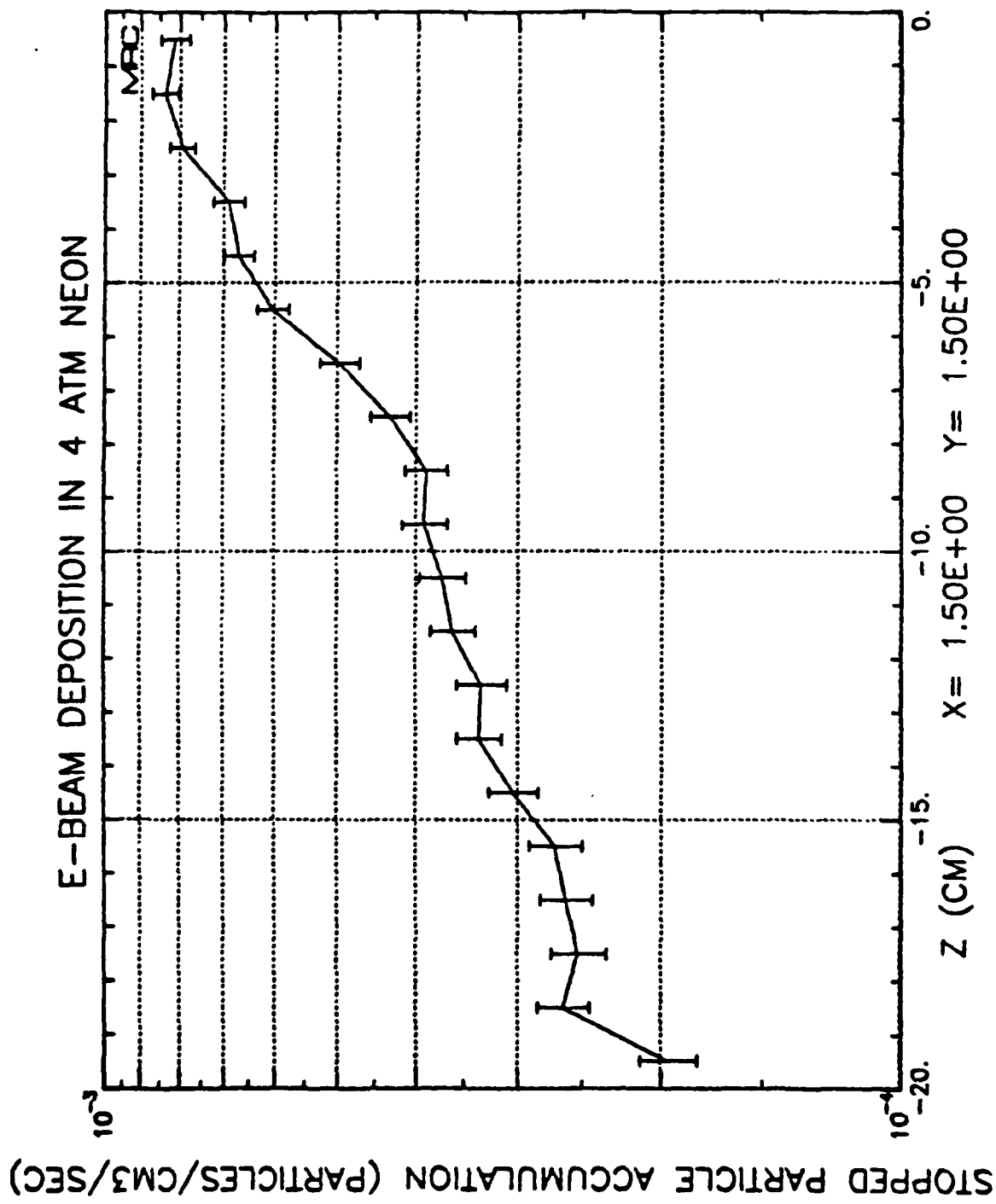
CASE NEON1M6B 25-JUL-80
Figure 9.



CASE NEON1M6B 25-JUL-80 09:25:27
Figure 10.

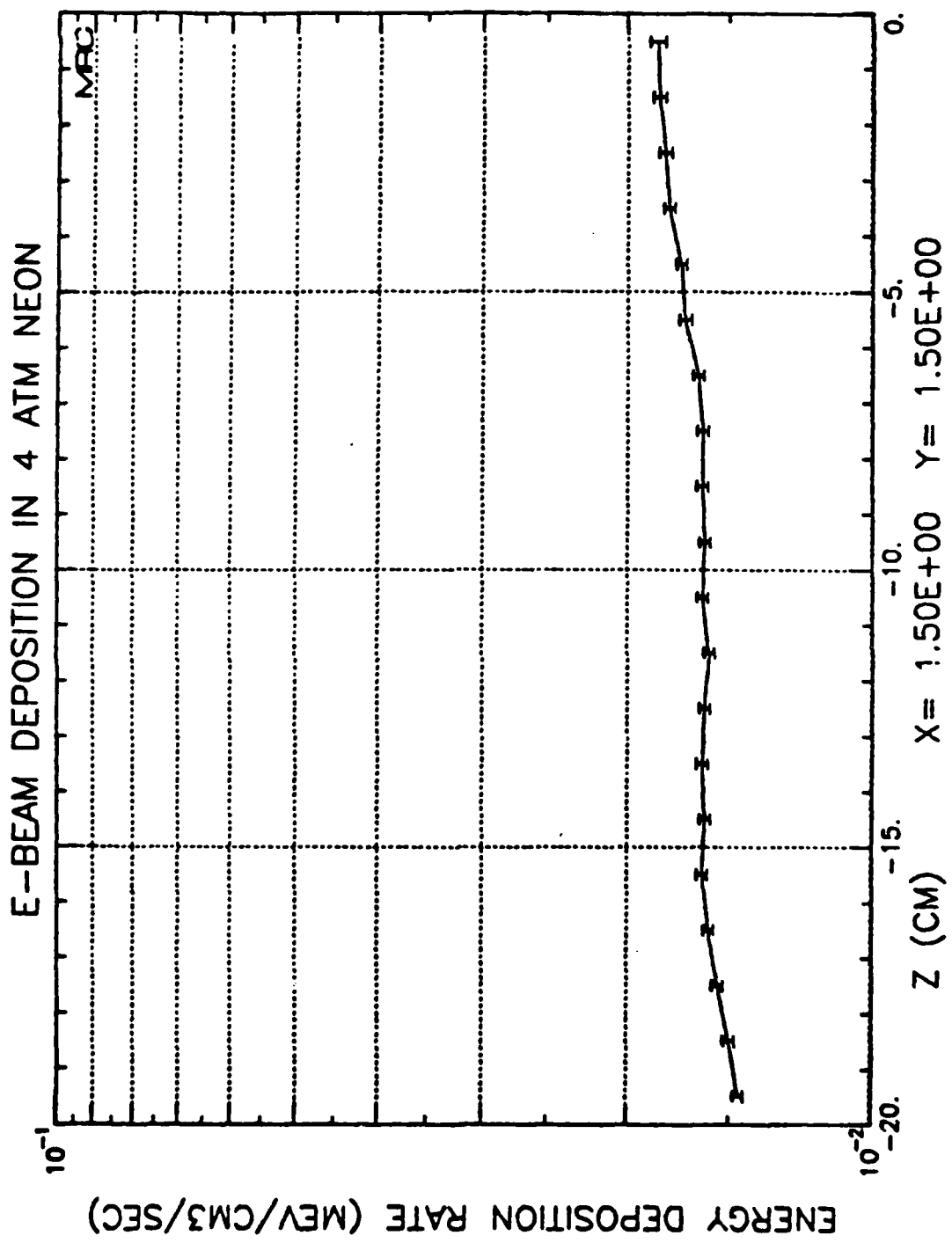


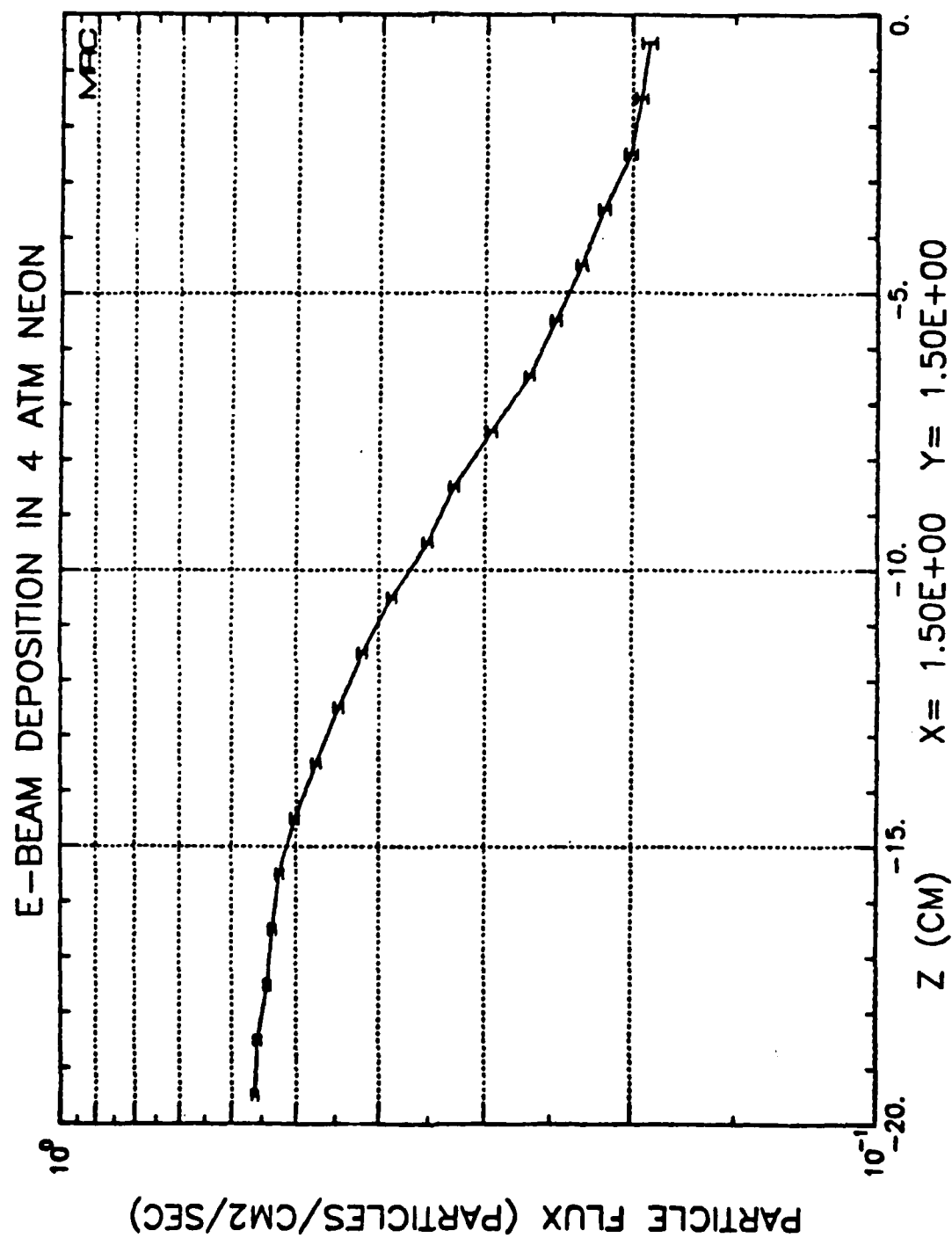
CASE NEON1M6B 25-JUL-80 09:27:23
 Figure 11.



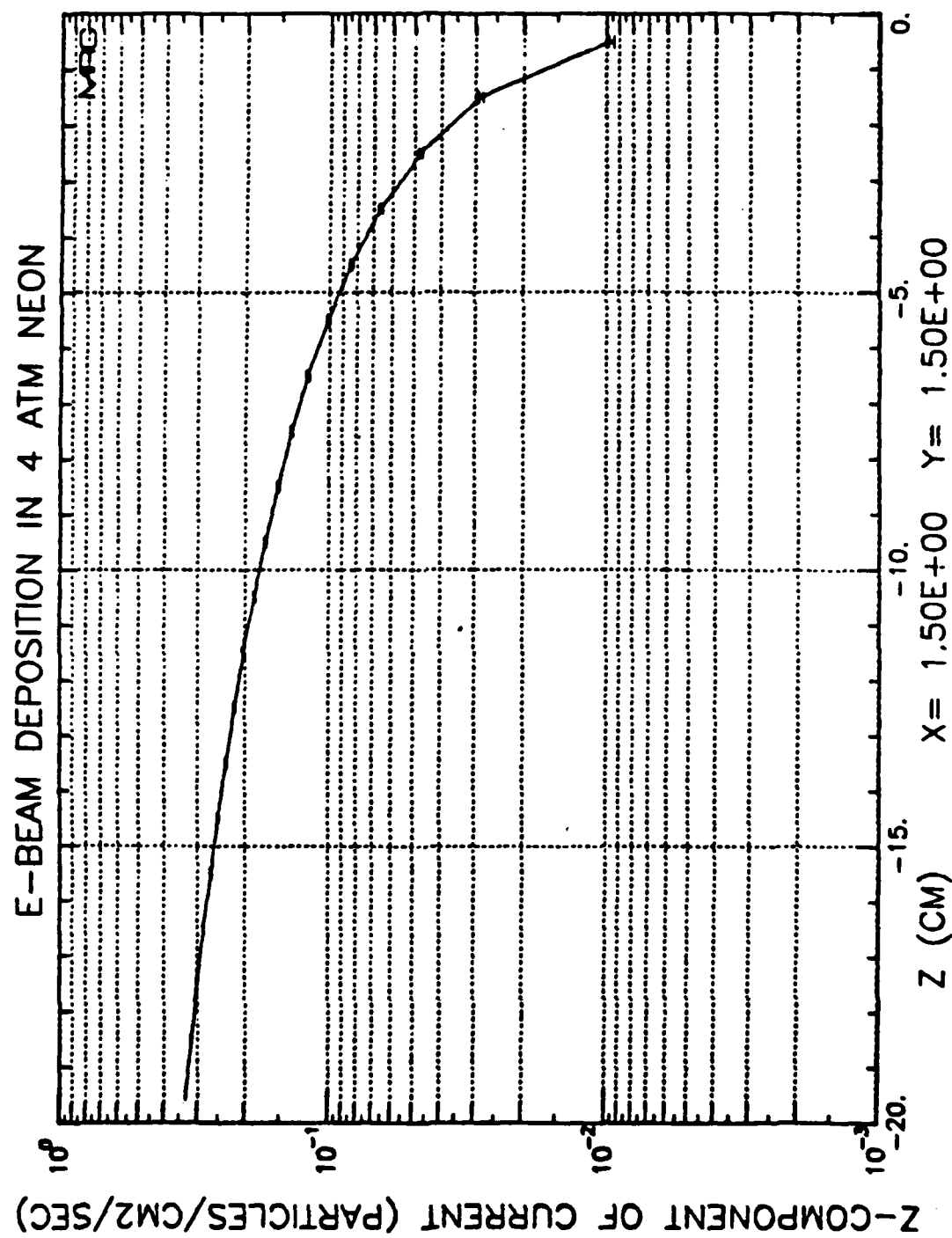
CASE NEON1M6B 25-JUL-80
Figure 12.

09:26:26

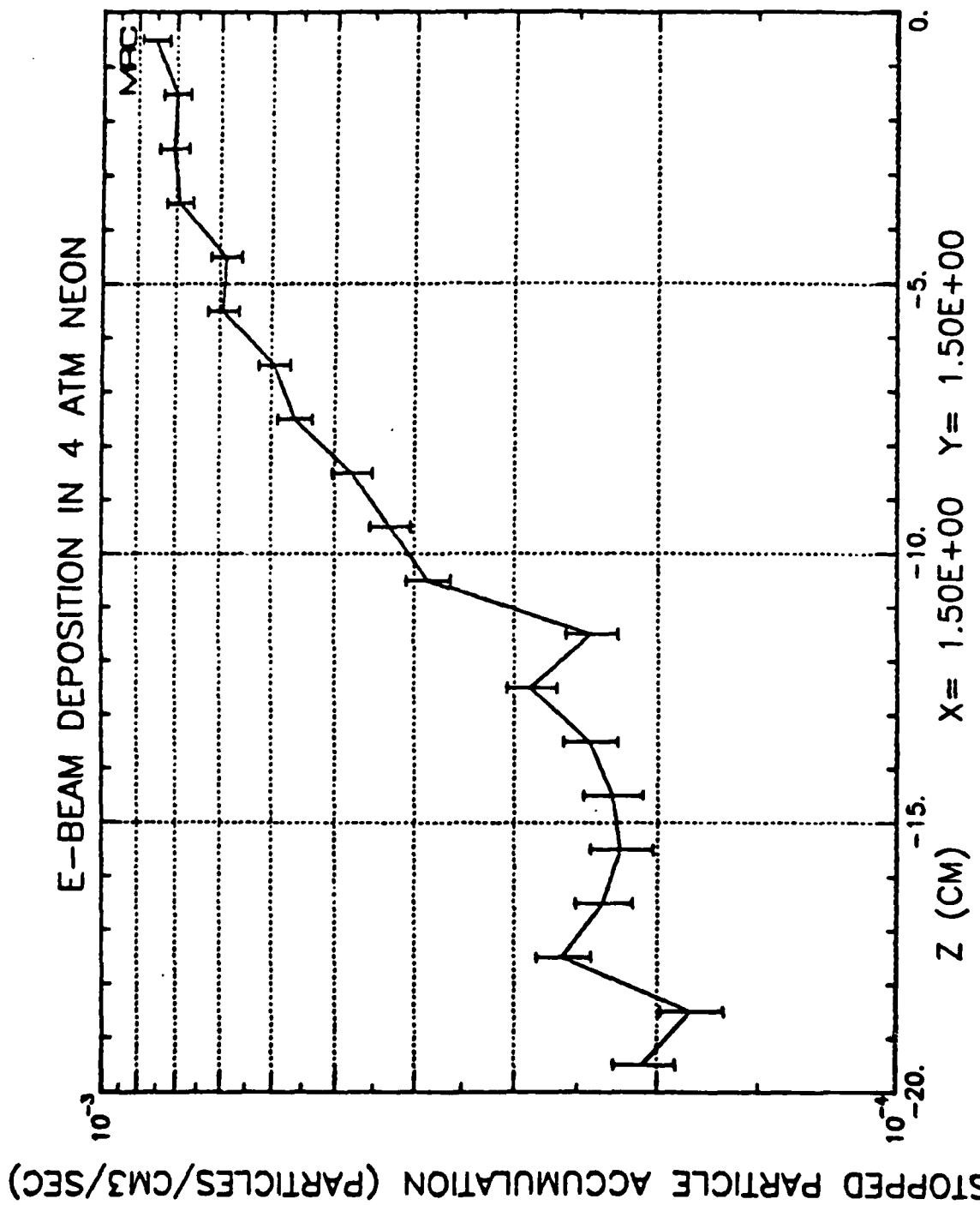




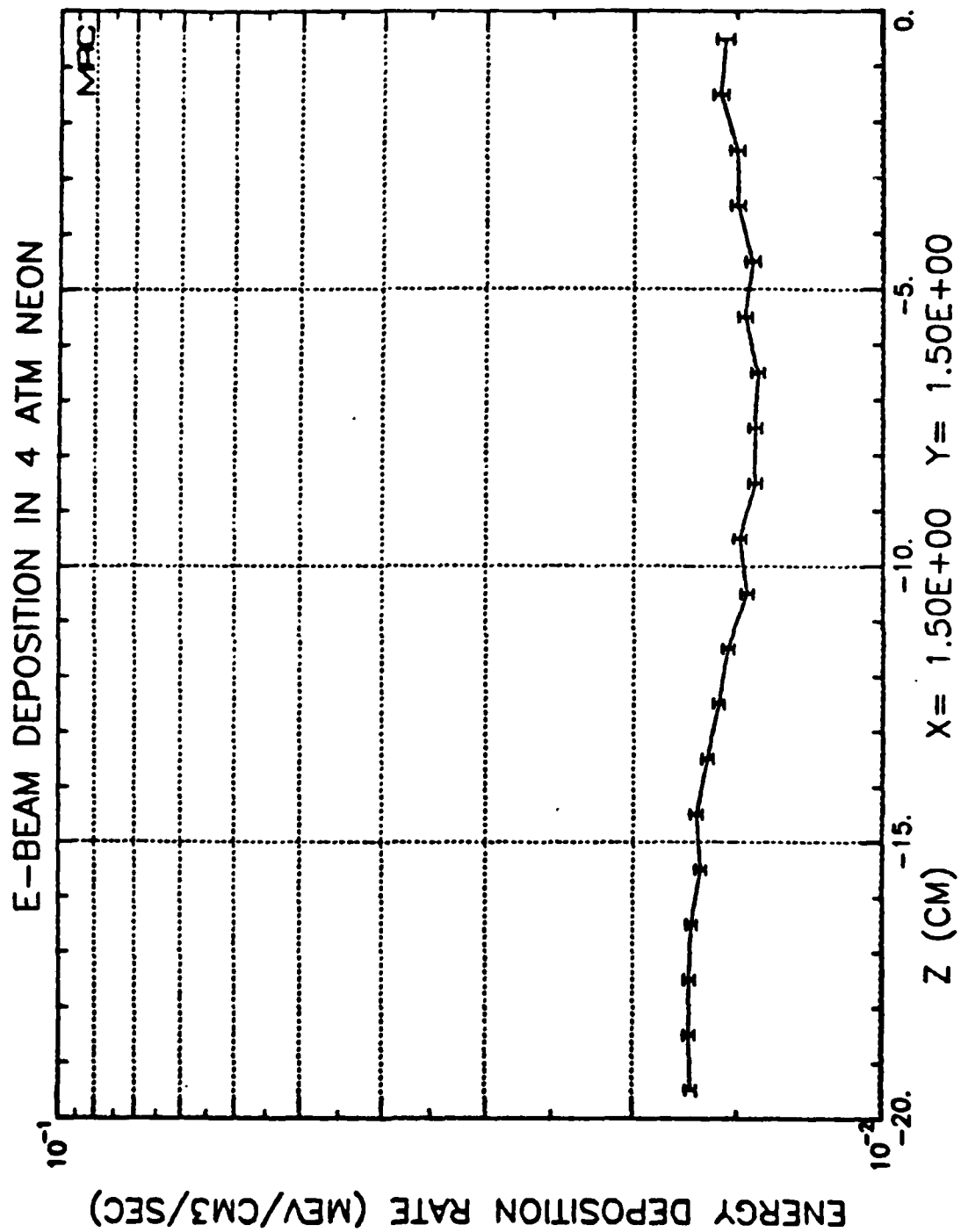
CASE NE1M6C X = 1.50E+00 Y = 1.50E+00
 Figure 14.



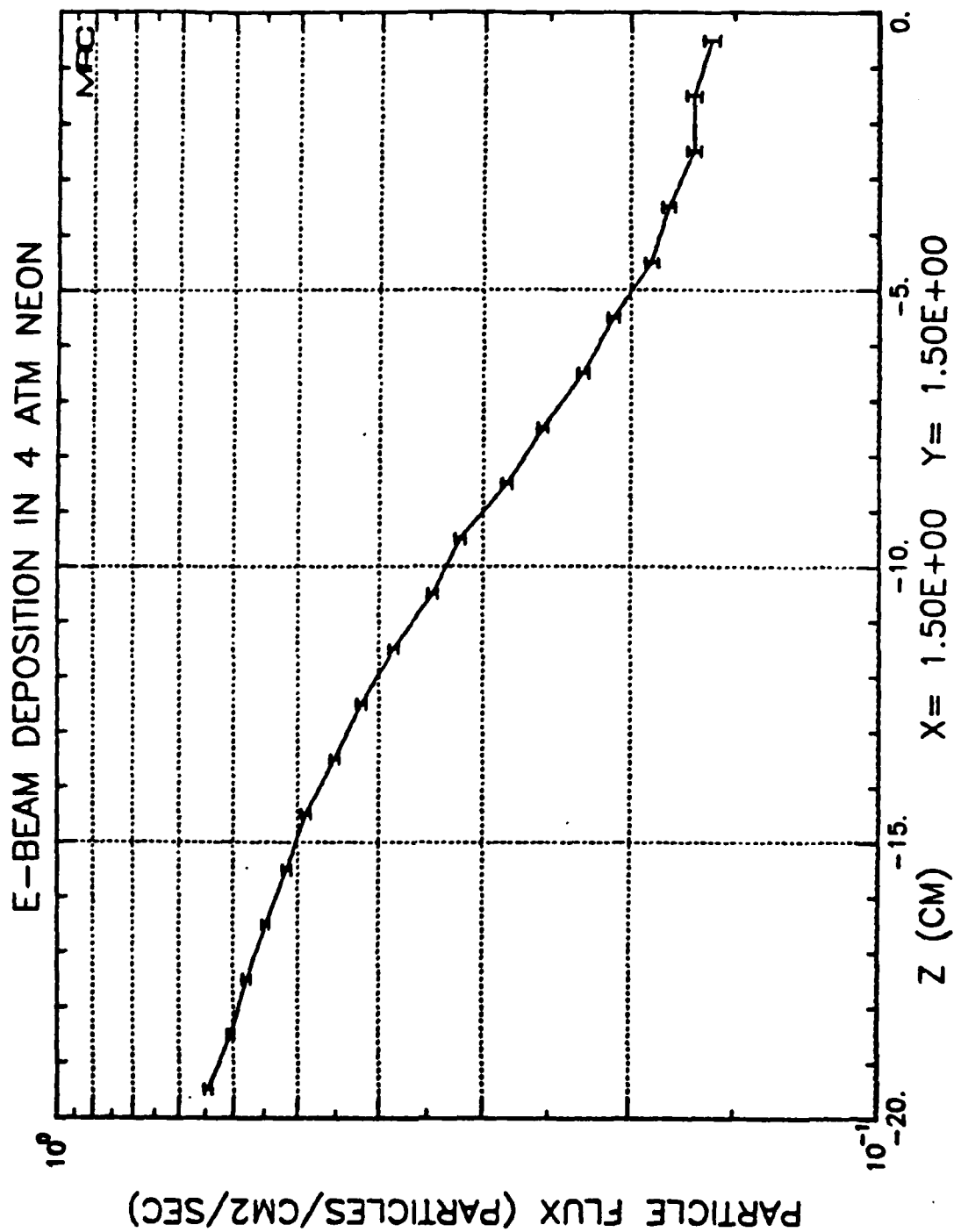
CASE NE1M6C 25-JUL-80 11:57:36
Figure 15.



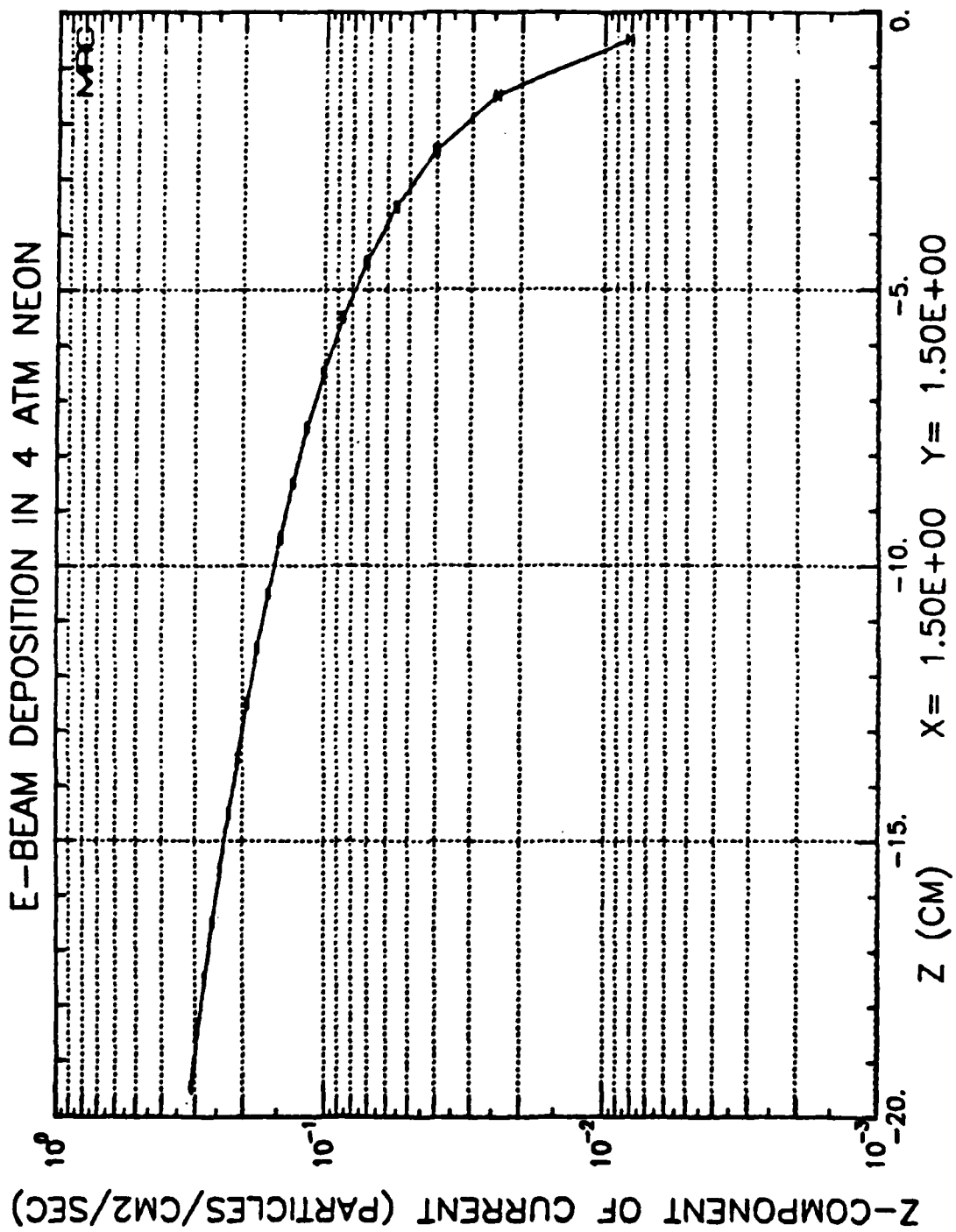
CASE NE1M6C 25-JUL-80 11:56:24
Figure 16.



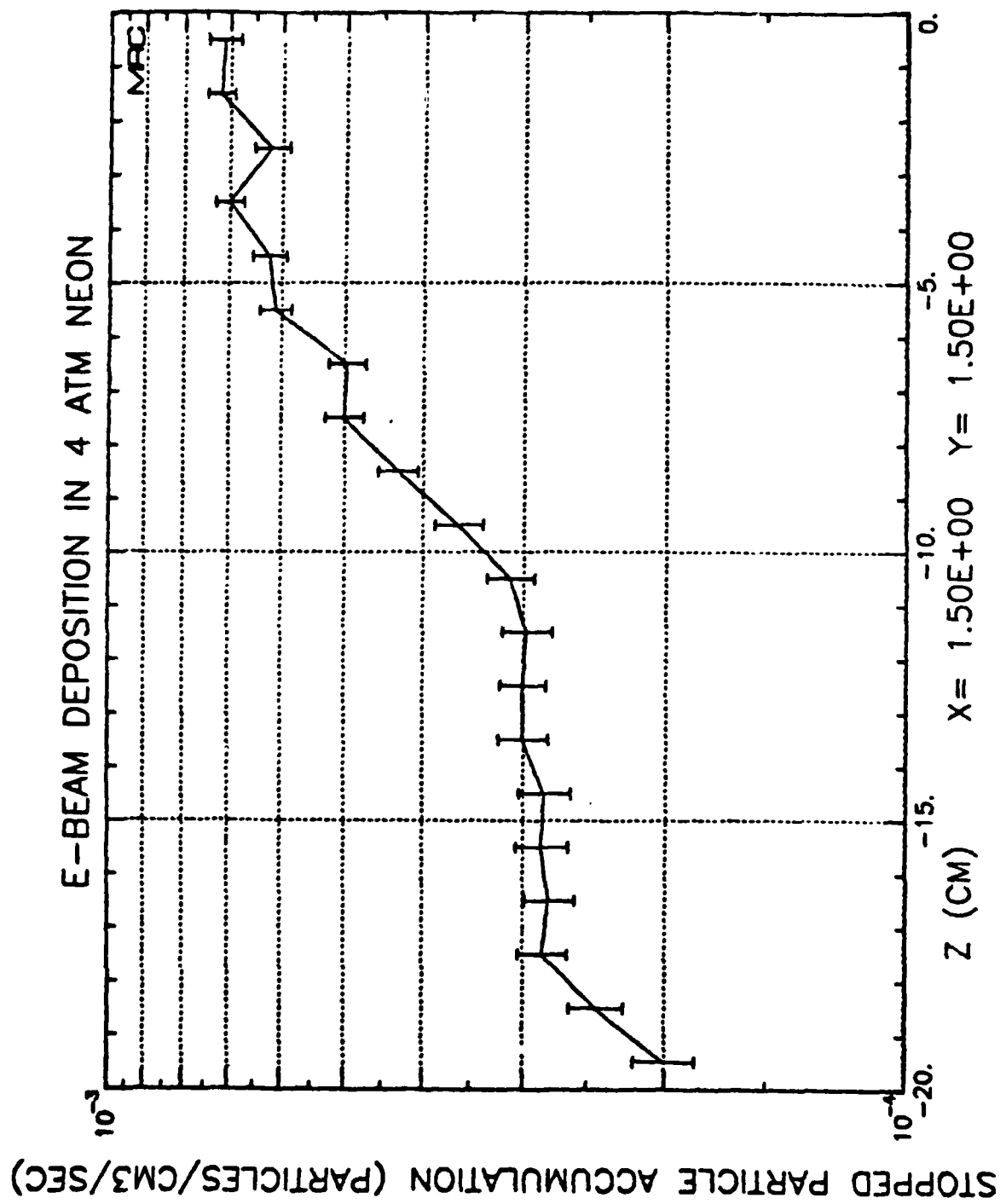
CASE NEON6B 25-JUL-80 09:32:20
Figure 17.



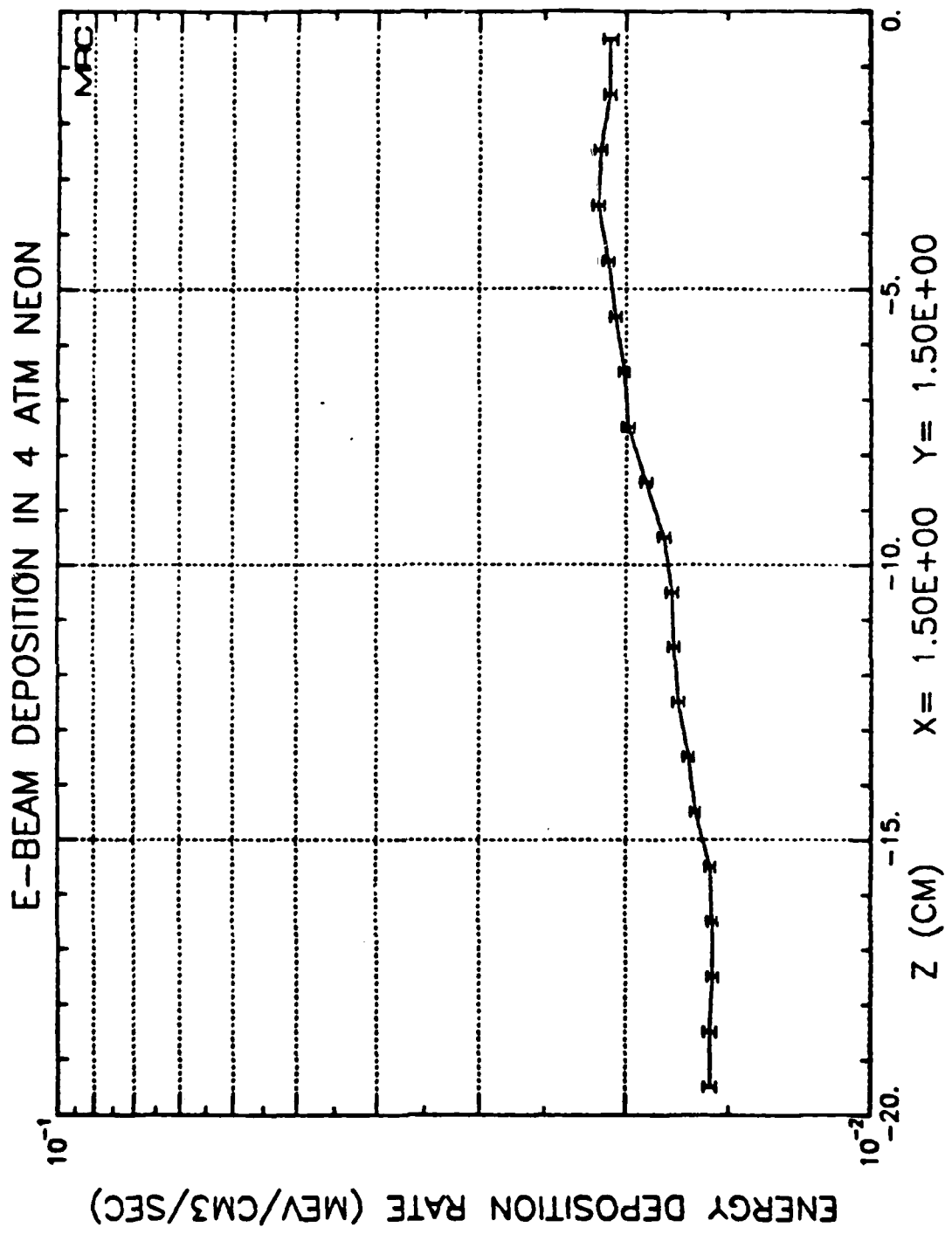
CASE NEON6B 25-JUL-80 09:33:25
 Figure 18.

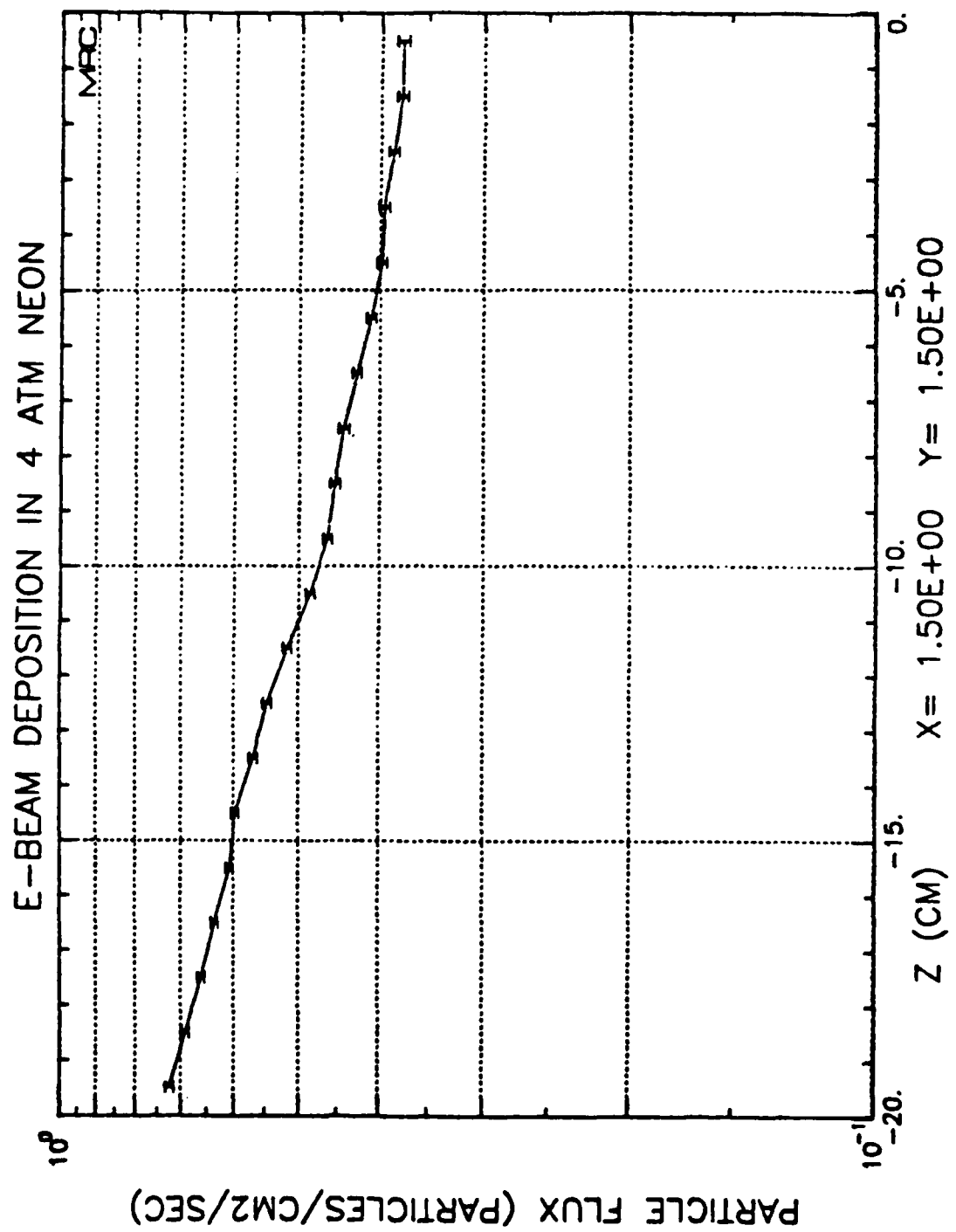


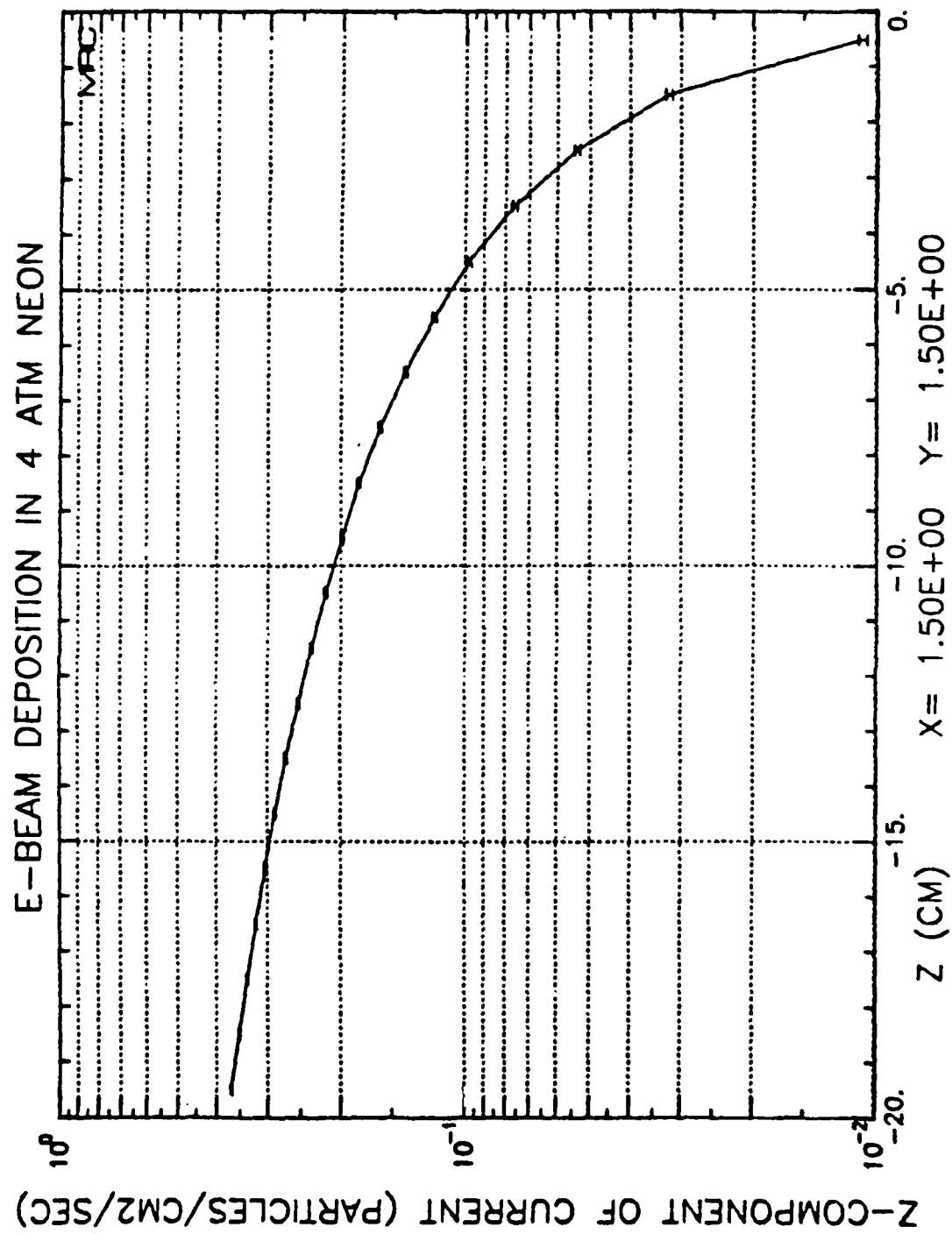
CASE NEON6B 25-JUL-80 09:35:24
Figure 19.



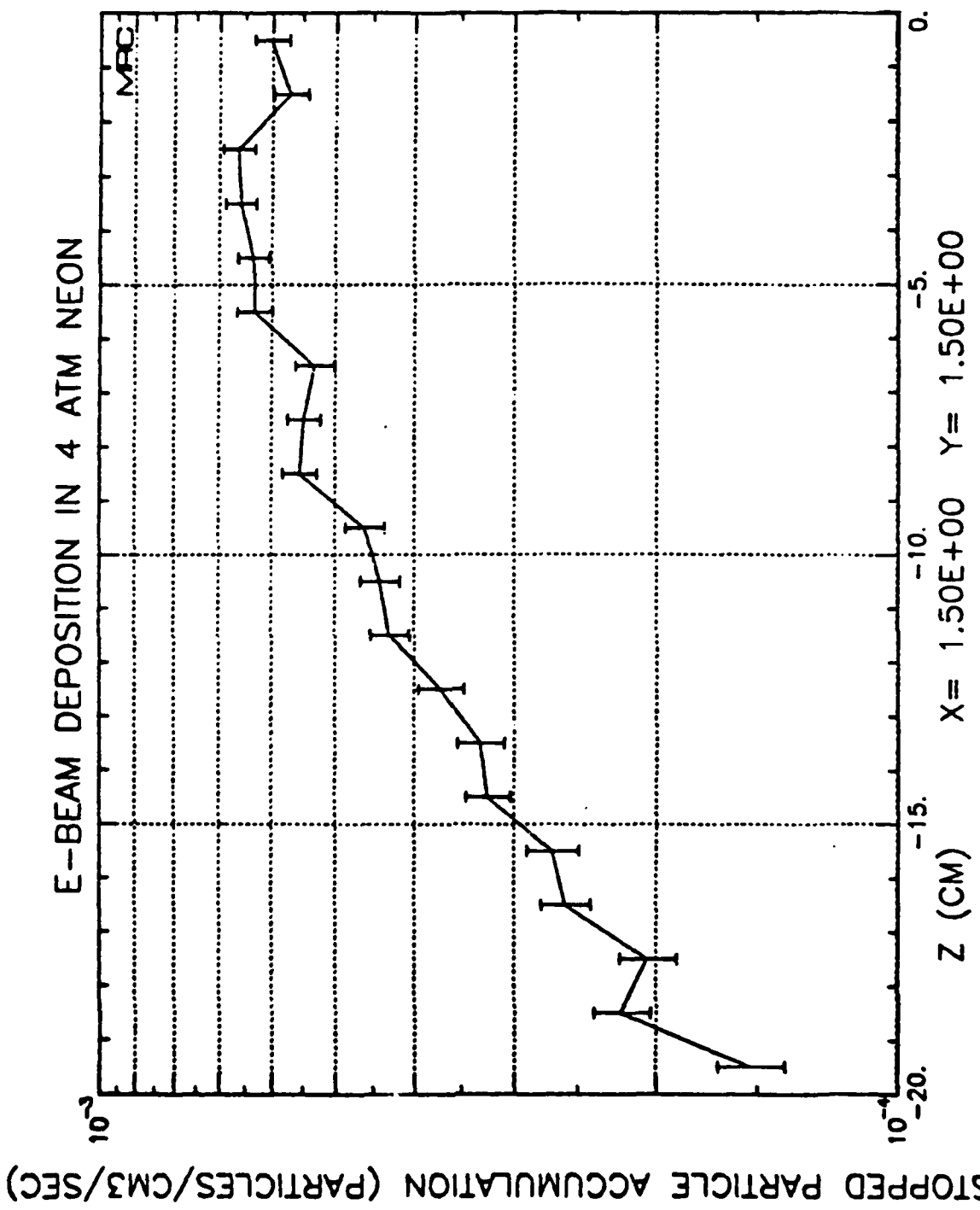
CASE NEON6B 25-JUL-80 09:34:26
Figure 20.



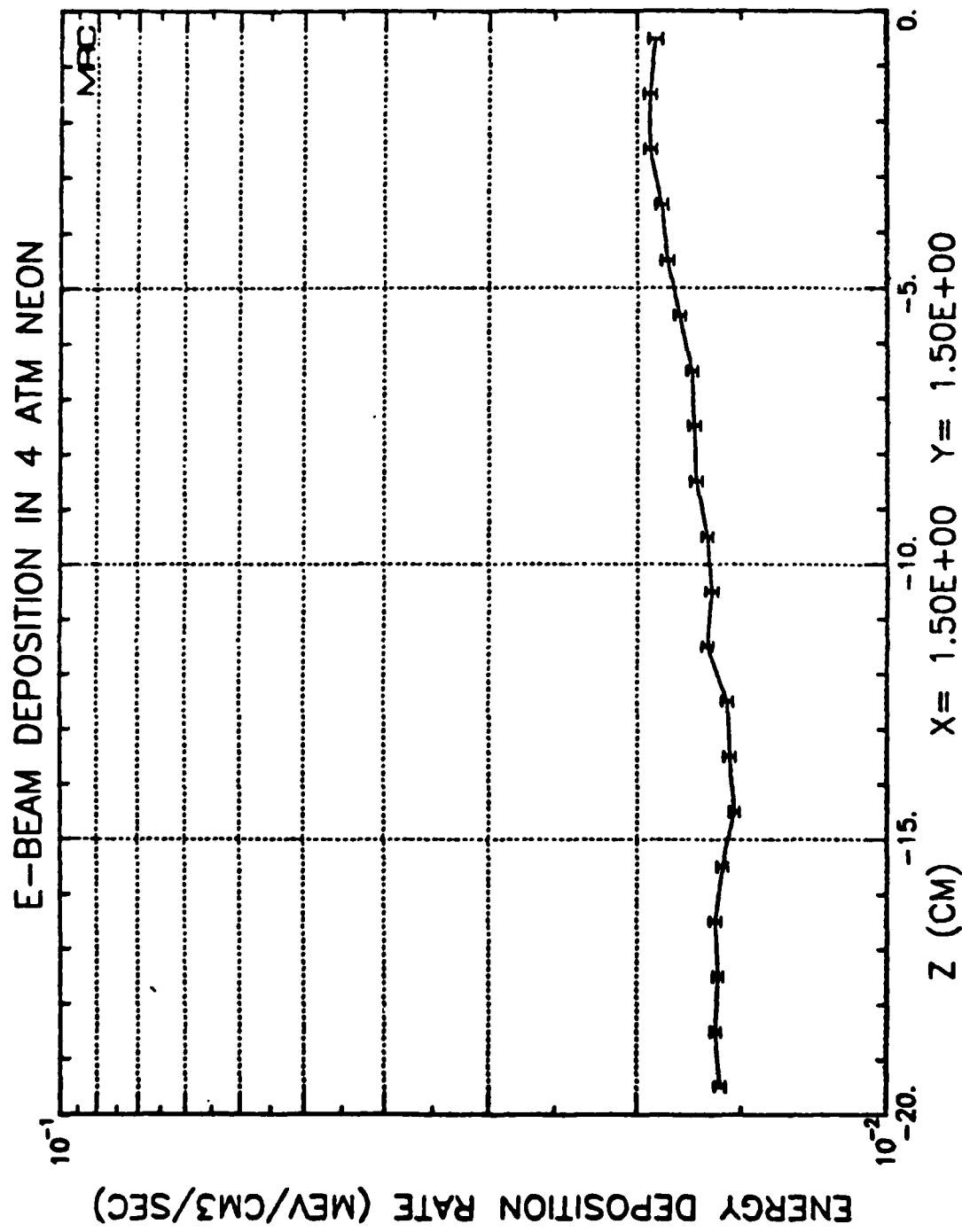




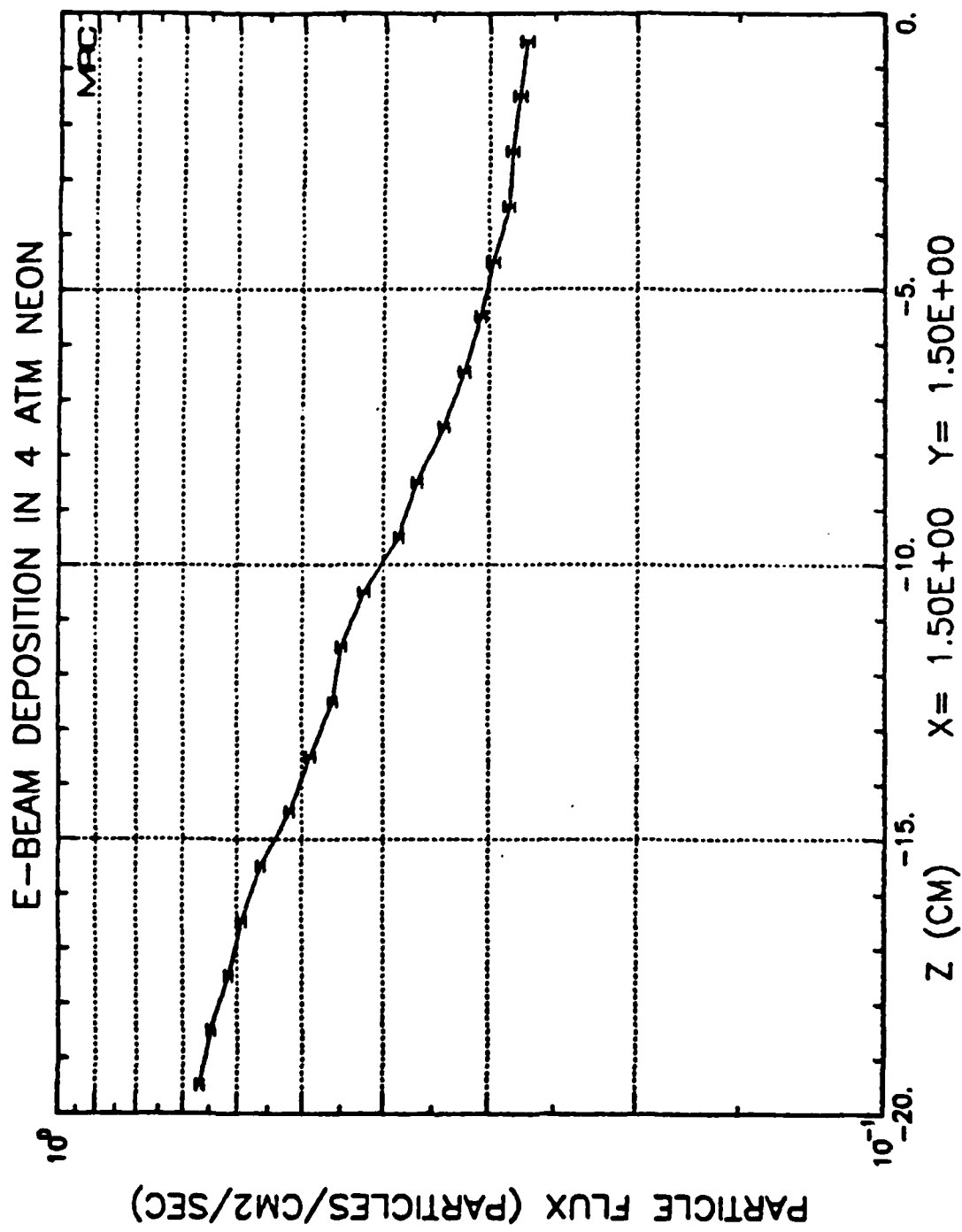
CASE NEON6C 24-JUL-80 16:18:33
 Figure 23.

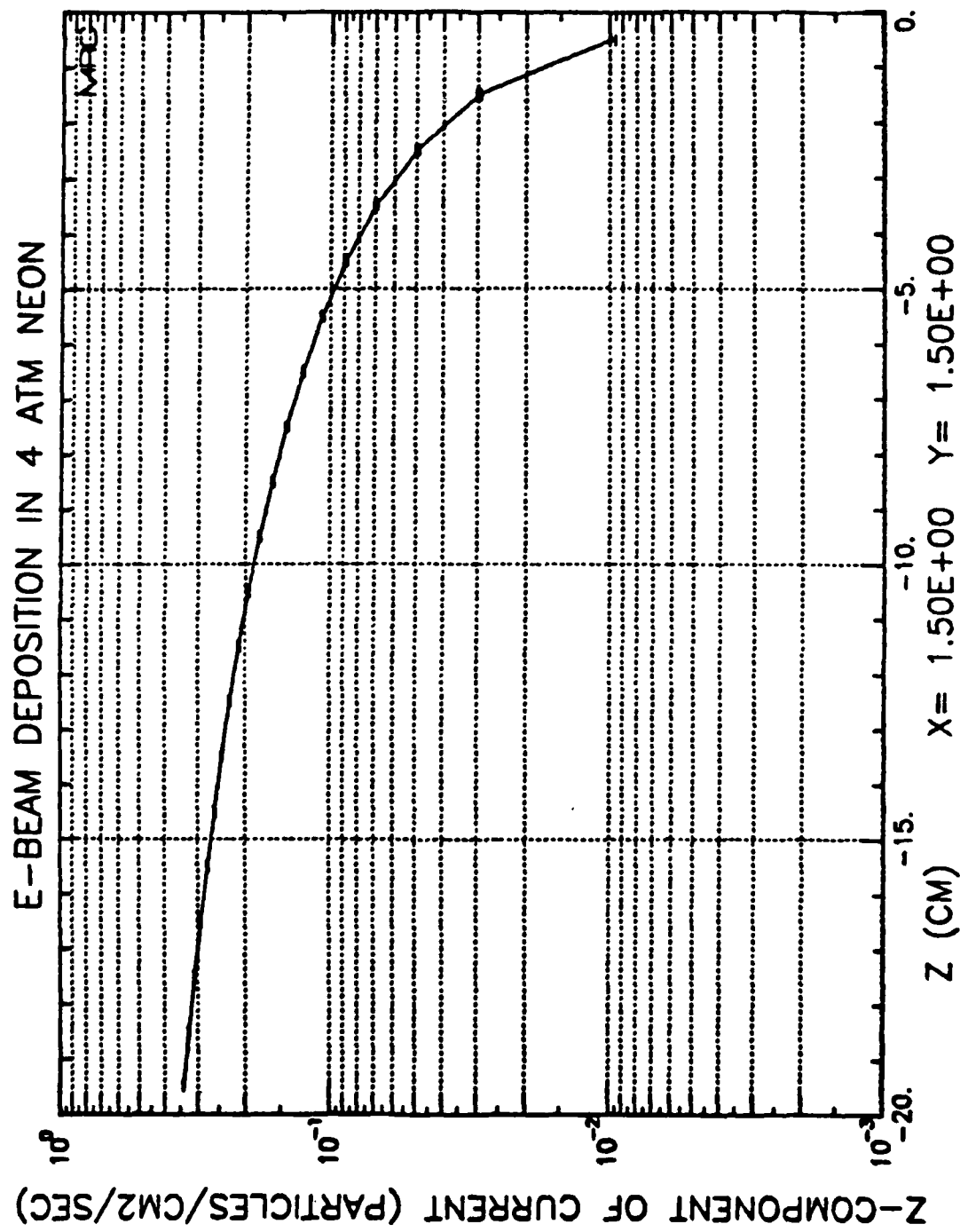


CASE NEON6C 24-JUL-80 16:17:23
Figure 24.



CASE NEON6D 25-JUL-80 16:07:13
Figure 25.





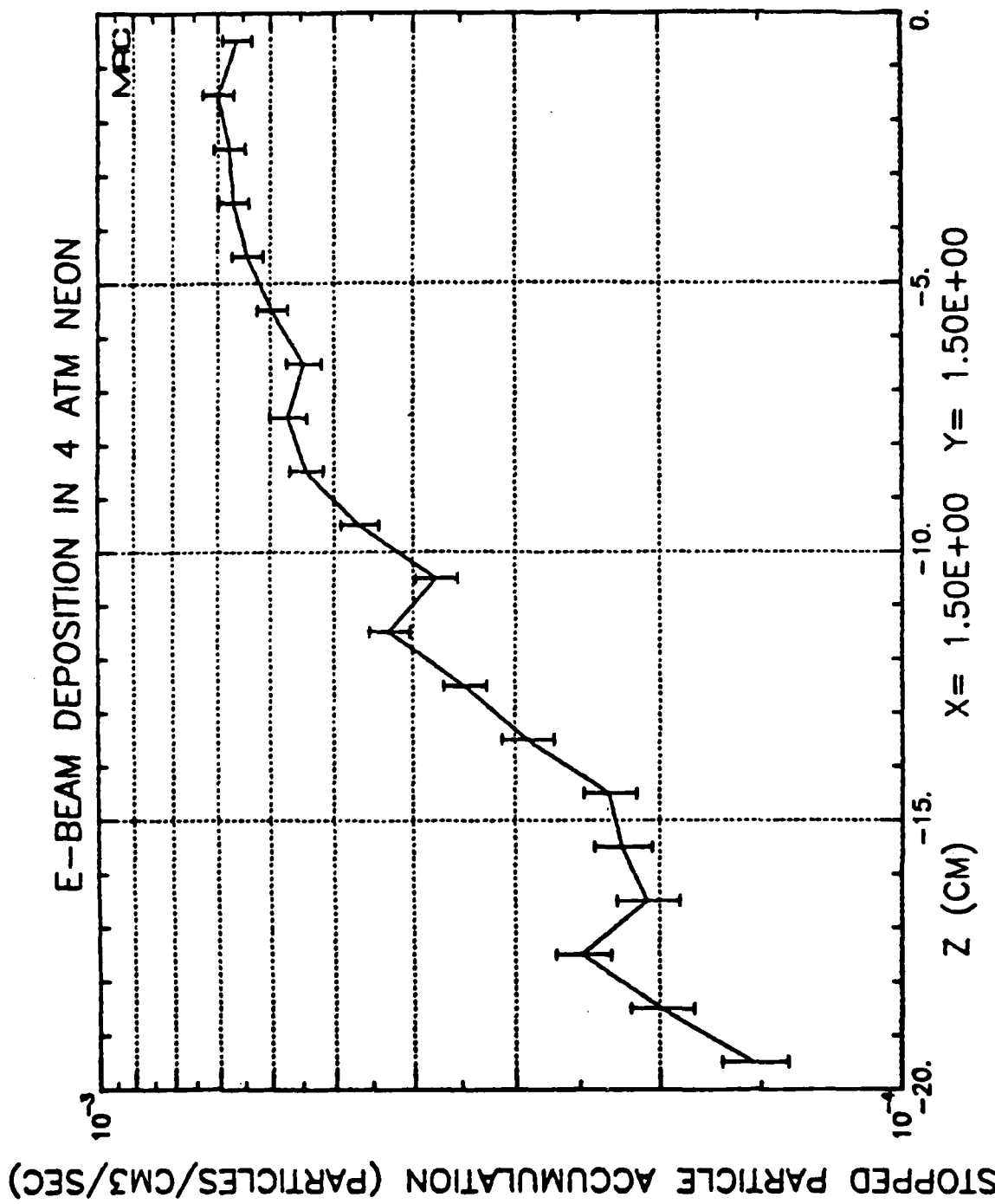


Table 1
Summary of Beam Centerline Deposition Calculations

<u>Case</u>	<u>Beam Energy (Kev)</u>	<u>Foil Thickness (Mil)</u>	<u>Injection Angle (Deg)</u>	<u>E_{max}</u>	<u>E_{min}</u>	<u>Uniformity</u>
1M6	400	1	0	202	155	0.26
1M6B	350	1	0	167	132	0.23
1M6C	375	1	0	184	146	0.23
6B	400	2	0	171	142	0.19
6C	450	2	0	216	157	0.32
6D	425	2	0	193	153	0.23

For the diode region, the ability to withstand the mechanical forces generated by foil failure is important. The foil support structure is of particular interest if high injection efficiency is desired. The suppression of stray ignition and nonuniform flows are both major design criteria. The magnetic field will provide an applied field to self field ratio of 8-10 and hence lead to good trajectory control. As far as the cathode behavior is concerned, the design problem is one of experience. Closure will not be a primary concern at this pulse length since the line will automatically compensate. The small area hot region near the edge will scatter out. Depending on the cathode structure (foil or felt) the filamentation of the electron flow in the collimating B field can be a problem.

Figure 29 shows the geometry for a 1 meter diameter planar diode with cylindrical geometry, indicating the emission area and Neumann boundary. Figure 30 shows the ratio of azimuthal to axial velocity at the anode plane in the cylindrically symmetric diode as a function of applied field and diode radius. Figure 31 shows the ratio of radial to axial velocity at the anode plane. In Figure 32, the current density versus radius for a 5 kilogauss guide field is shown, and in Figure 33 the plot of electron trajectories and equipotential lines is shown.

In summary, then, for the cathode behavior, if the voltage varies by ± 0.10 , closure rates of 1.5 cm/ μ s are acceptable. The preferred operation would be to start at higher voltage and run down to lower. Maxwell Labs data on felt and spark cathodes is of interest, and showed acceptable performance for felt.

Electrical Driver Design

It is desirable to keep the voltage fairly uniform in time and to match to the diode closure, if necessary. The driver size (70-100 KJ) is appreciable. It is of a size typical for a module, even if a much larger beam were desired.

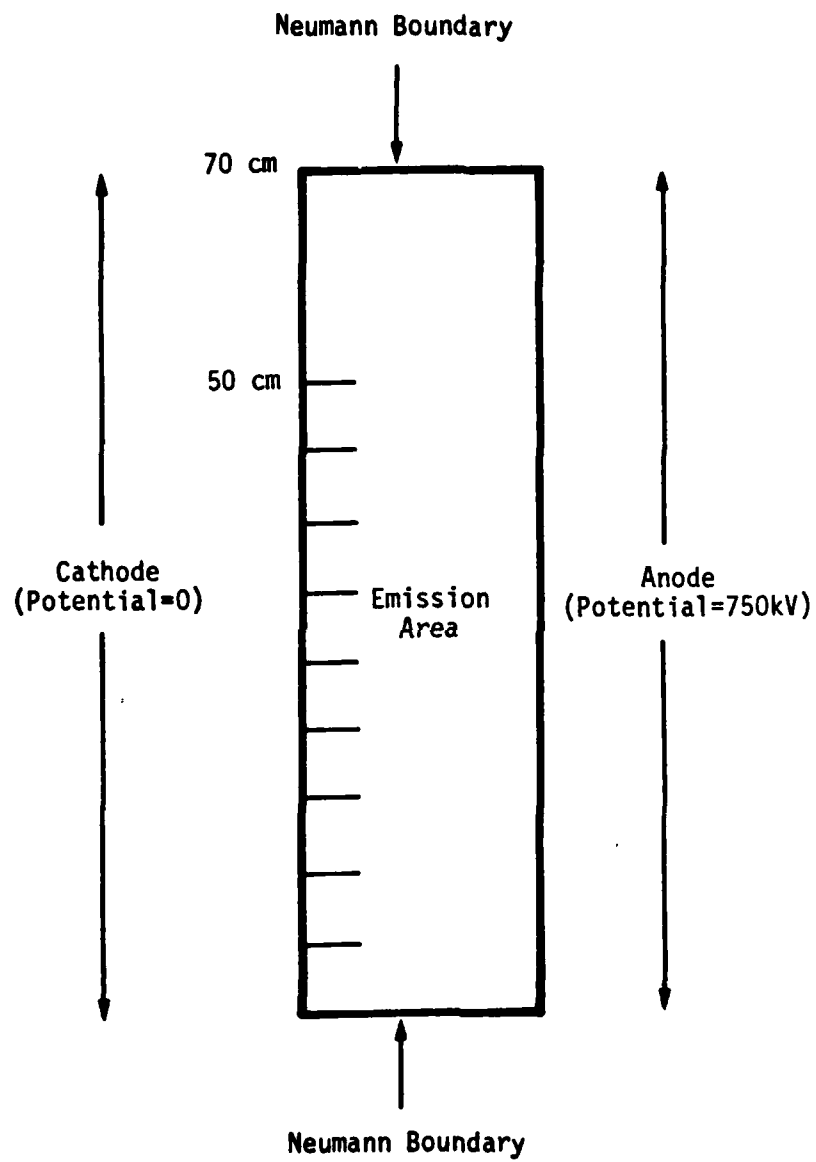


Figure 29. Geometry for one-meter diameter planar diode with cylindrical geometry.

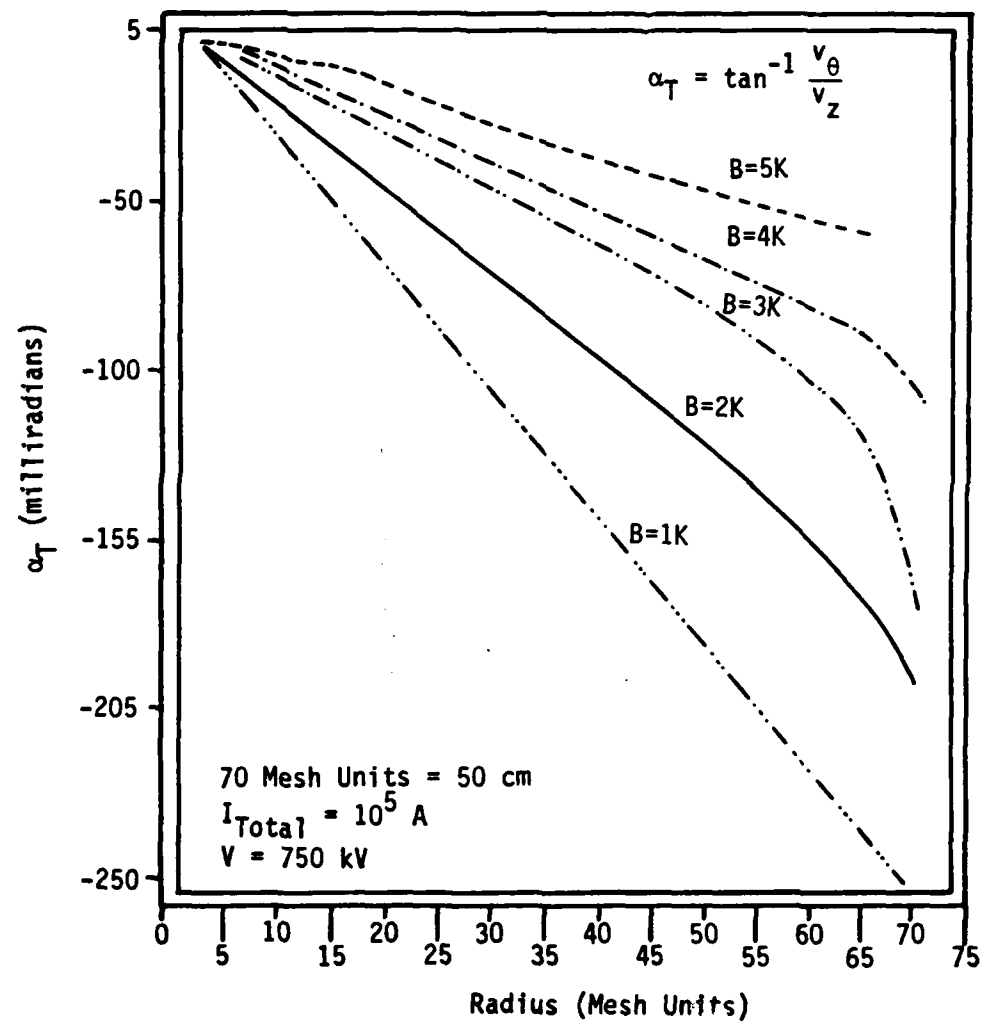


Figure 30. Ratio of azimuthal to axial velocity at anode plane in cylindrical diode as a function of applied field.

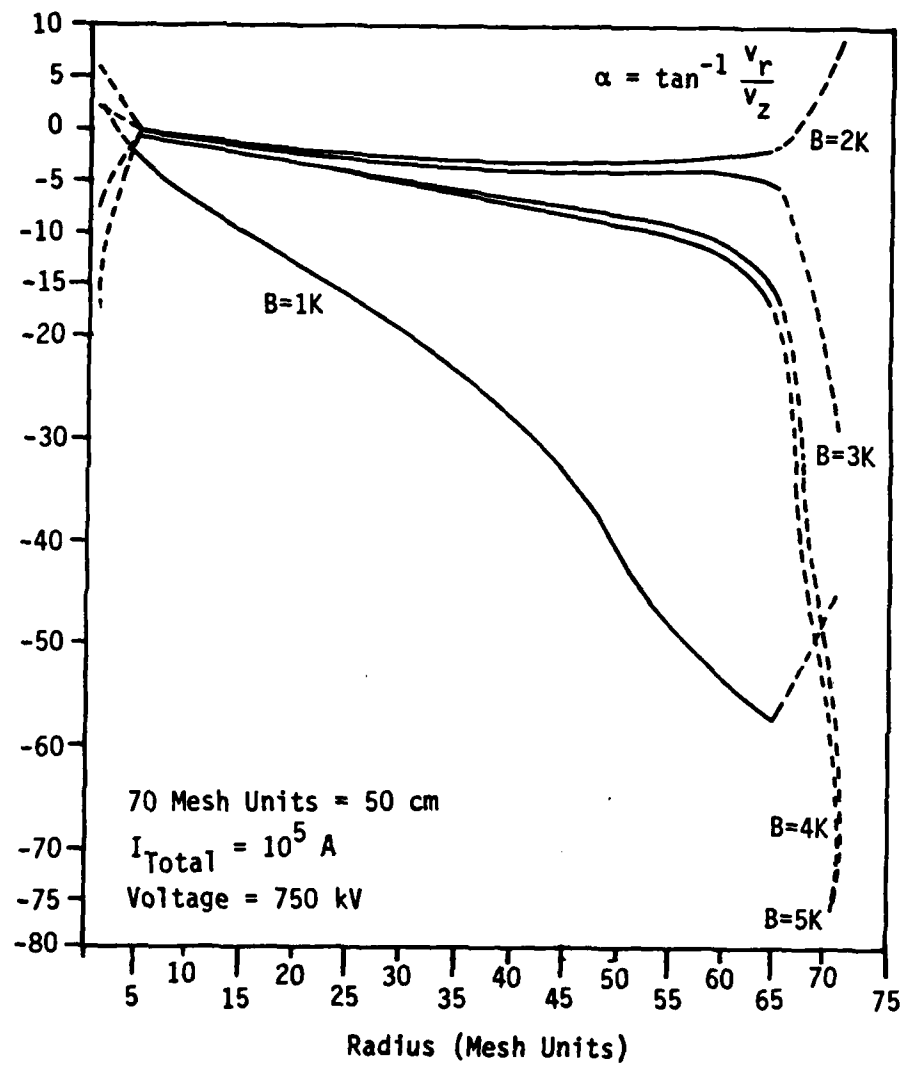


Figure 31. Ratio of radial to axial velocity at anode plane in cylindrical diode as a function of applied field.

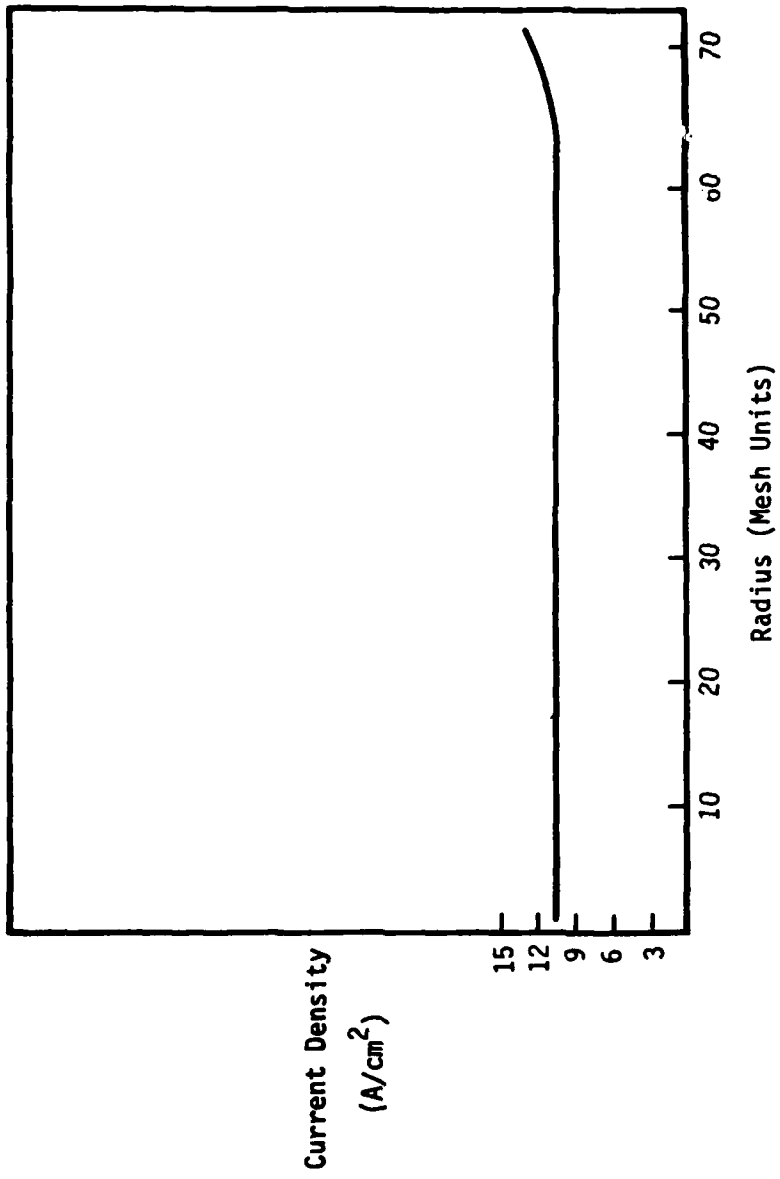


Figure 32. Current density vs. radius for a 5 kG guide field.

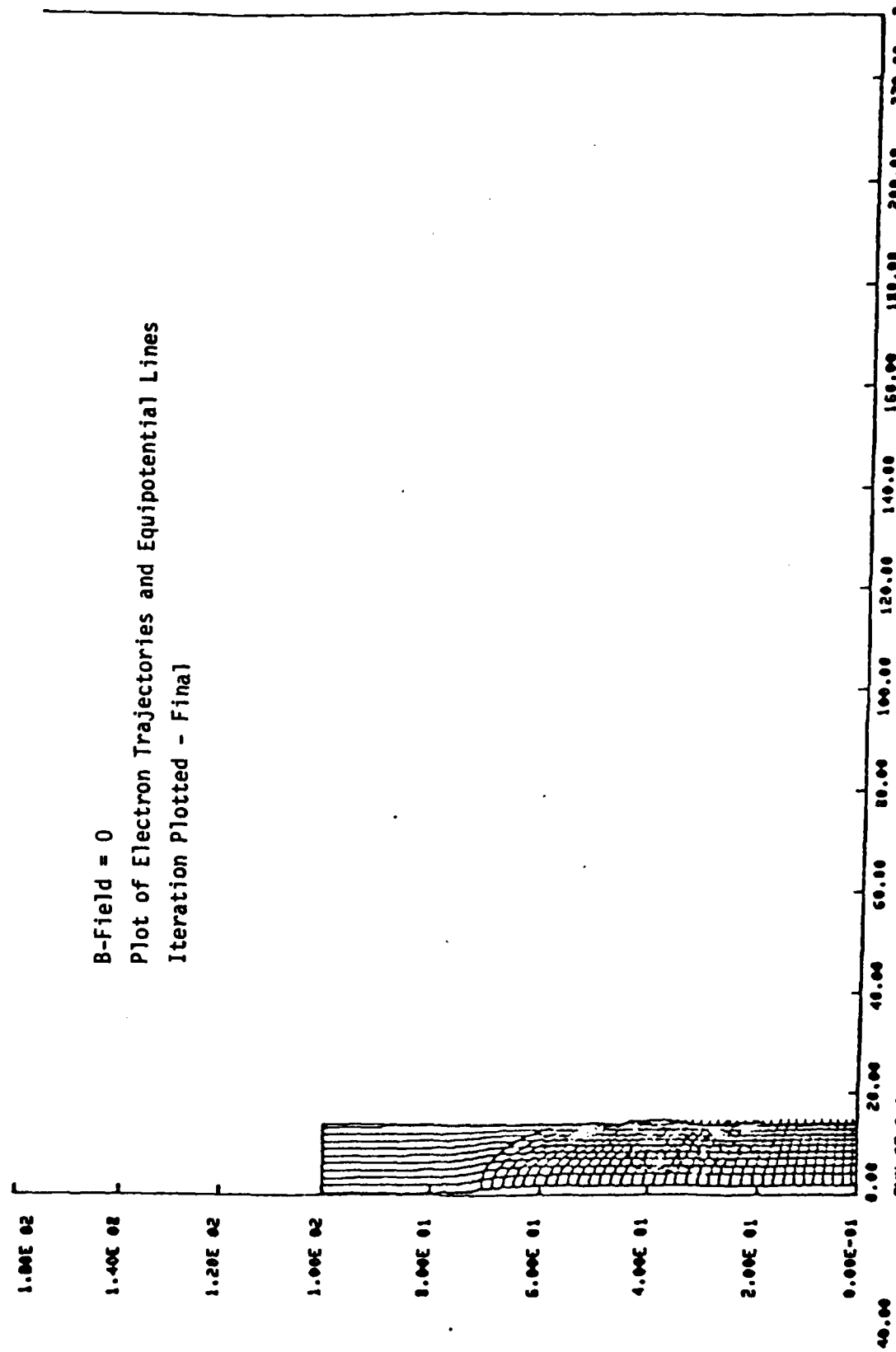


Figure 33. Plot of electron trajectories and equipotential lines.

Marxes may be divided into three classes: very fast, fast, and moderate speed. Very fast Marxes have inductances of less than 1 μ H/megavolt. They require compact packaging, usually requiring plastic cased capacitors, and cost in excess of \$1.50 per delivered joule. Fast Marxes have inductances of 1-3 μ H/megavolt. These are also compact in geometry, but utilize metal cased capacitors, costing in the range of \$.50 to \$1.00 delivered joule. The moderate speed Marxes have inductances in excess of 3 μ H/megavolt. These are typical of large energy storage Marxes, costing about \$0.40 per delivered joule.

Figure 34 shows plots of PFN energy as a function of pulse length for several different speed Marxes. Figure 35 shows several different driver types, including lumped PFN's and pulse charged water lines (distributed, lumped, and staged). Figure 36 shows a schematic of a water driver diode, and Figure 37 shows a computer model of a pulse charged lumped element line. In Figure 38 load parameters for the pulse charged lumped element line are plotted and in Figure 39 the costs for the different drivers are shown in per joule as a function of pulse length. This last figure was composed assuming large volume production.

In terms of reliability, the prime concerns are the demonstrated component performance under normal operation as well as under operating faults. One aspect of the design then includes the energy in the driver foil that can withstand a fault. We prefer less than 50 KJ stored per side as a single driver. Fault currents and reversal are within reasonable practice in this case ($\sim 6 \Omega$, 800 KV open circuit). This is the area of primary interest in the circuit design. The key is repeated operation (several 100 short sequences) of the device with $< .03$ failure rate. The old NRL beam would do this.

A magnetic field of ~ 1 kilogauss over the diode and chamber regions with a uniformity better than ± 0.05 is necessary to collimate the

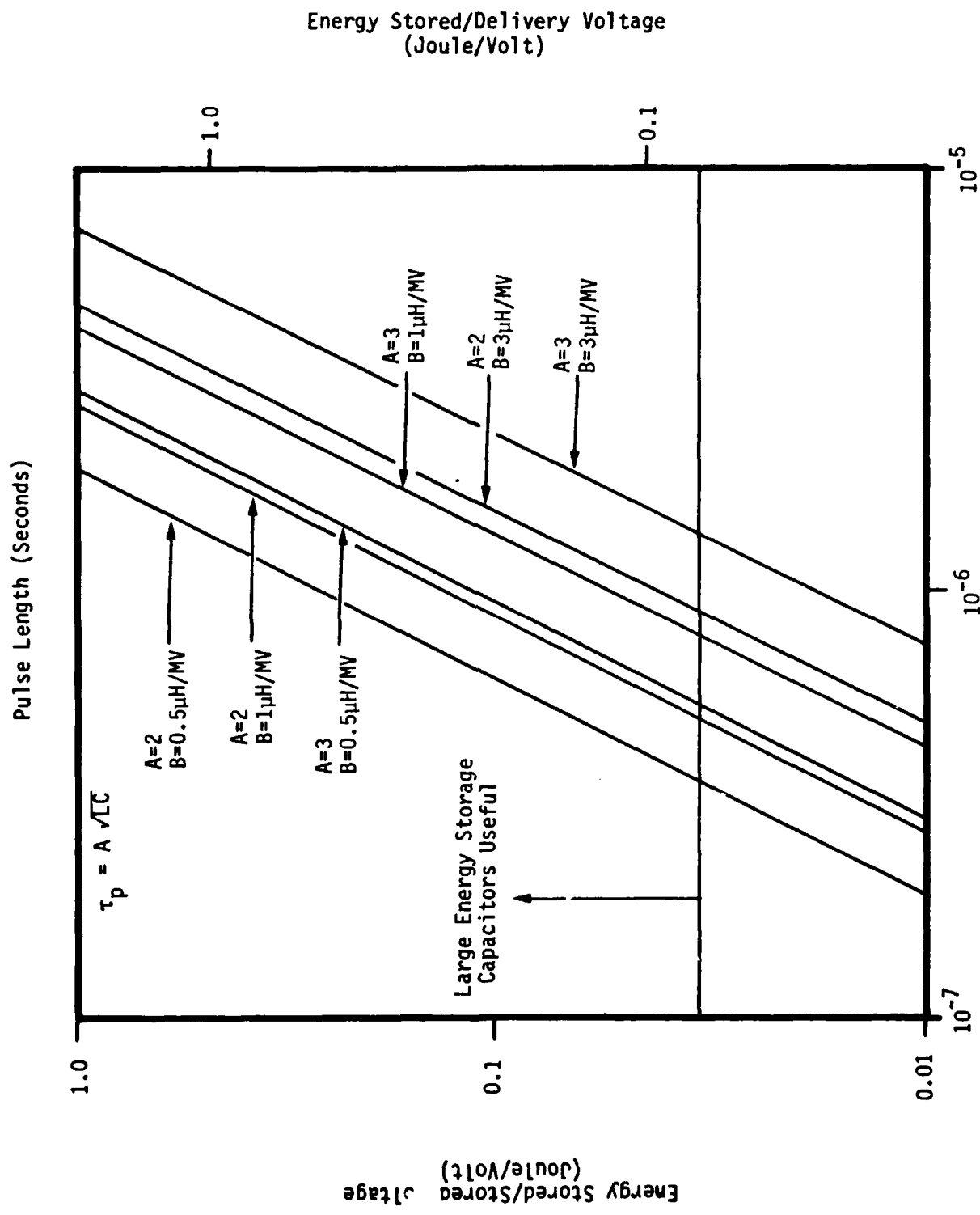
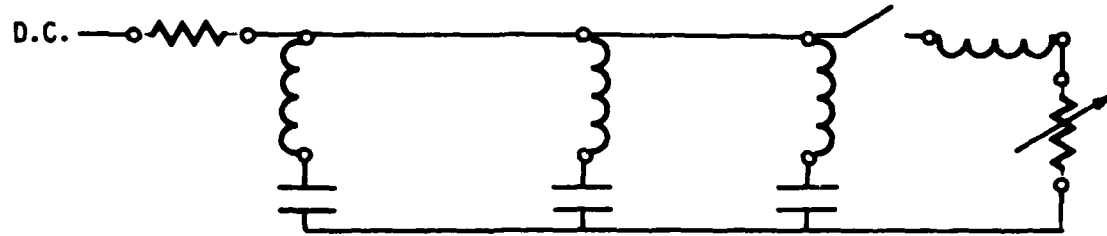


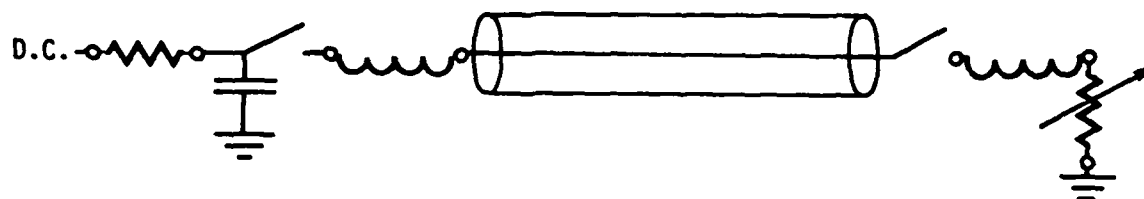
Figure 34. Pulse forming network energy as a function of pulse length for several different speed Marxes.

LUMPED ELEMENT PFN's

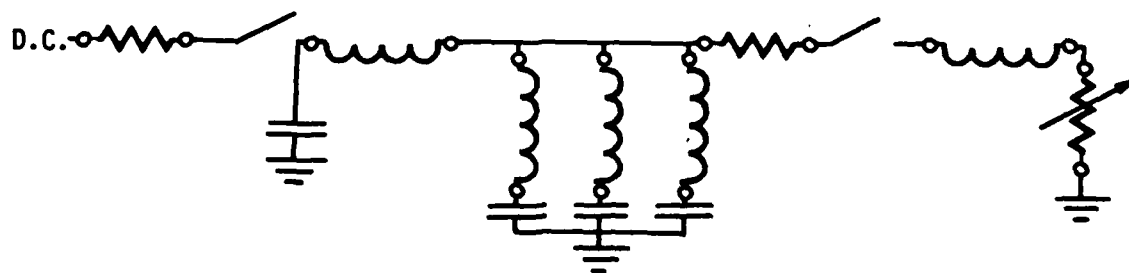


PULSE CHARGED H₂O LINES

Distributed



Lumped



Staged

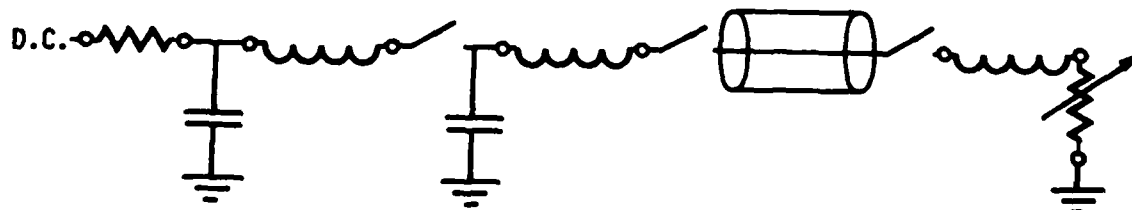


Figure 35. Classes of electrical drivers.

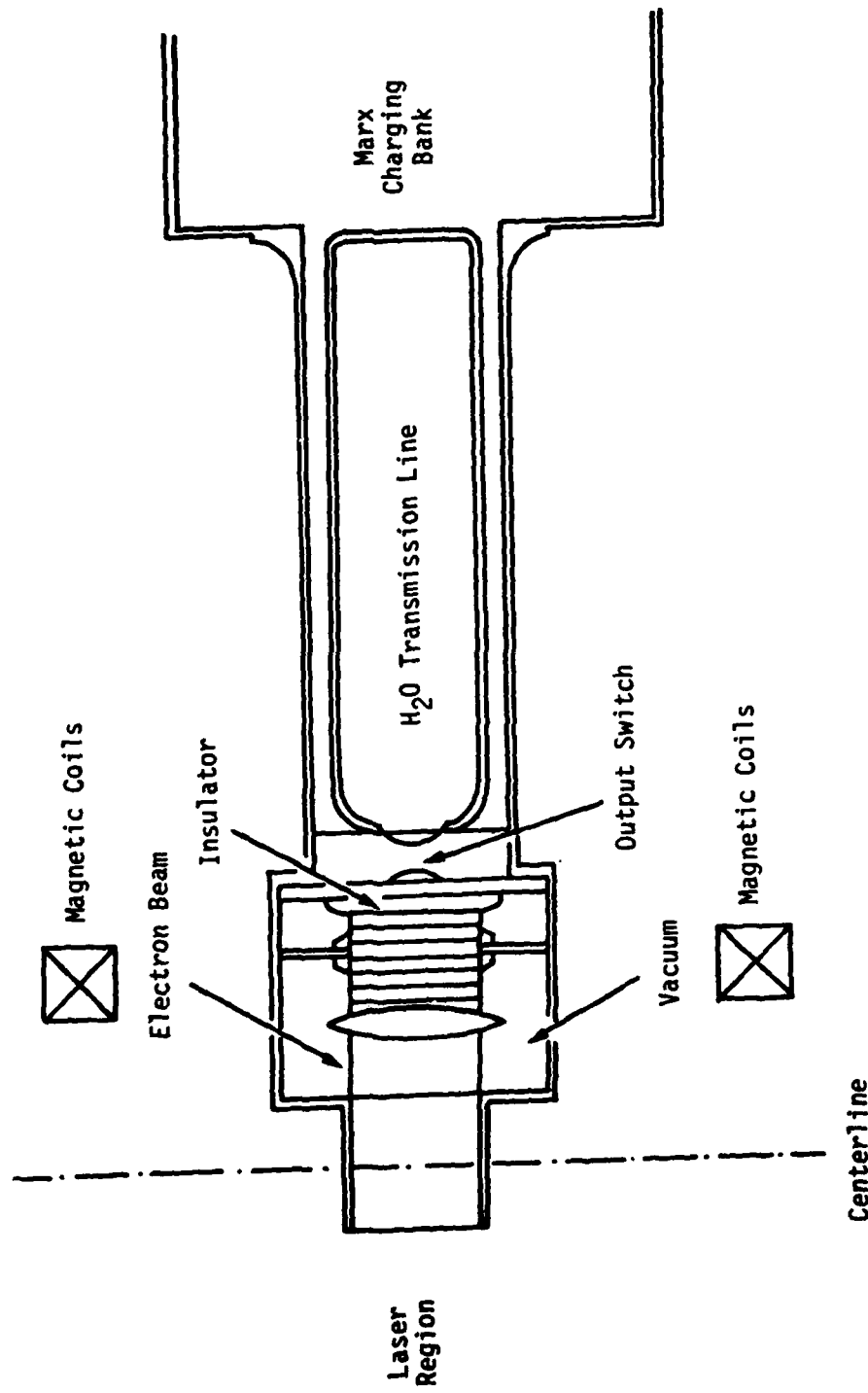
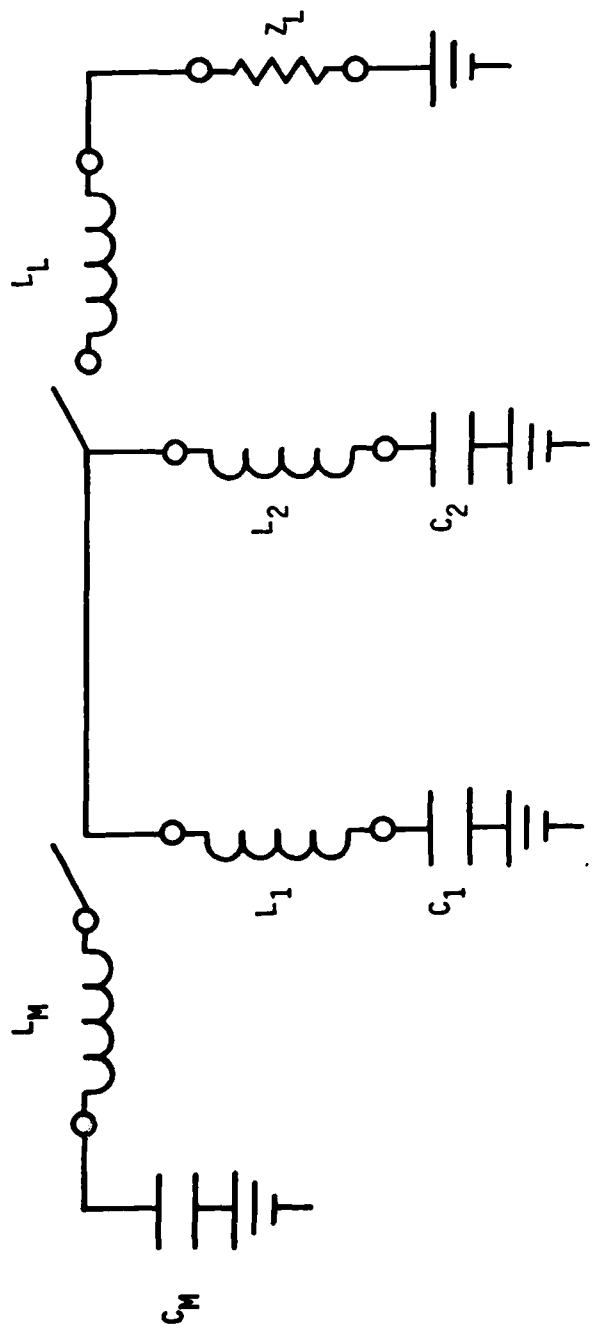


Figure 36. Schematic of diode driven by water.



Values:	$L_M = 10^{-6}$ Henrys	$L_1 = 474 \times 10^{-9}$ Henrys
	$C_M = 0.9 \times 10^{-7}$ Farads	$L_2 = 506 \times 10^{-9}$ Farads
	$Z_L = 3.75$ Ohms	$C_1 = 53.3 \times 10^{-9}$ Farads
	$L_L = 10^{-7}$ Henrys	$C_2 = 5.33 \times 10^{-9}$ Farads

Figure 37. Computer model of pulse charged lumped element line (class C - pulsed charge).

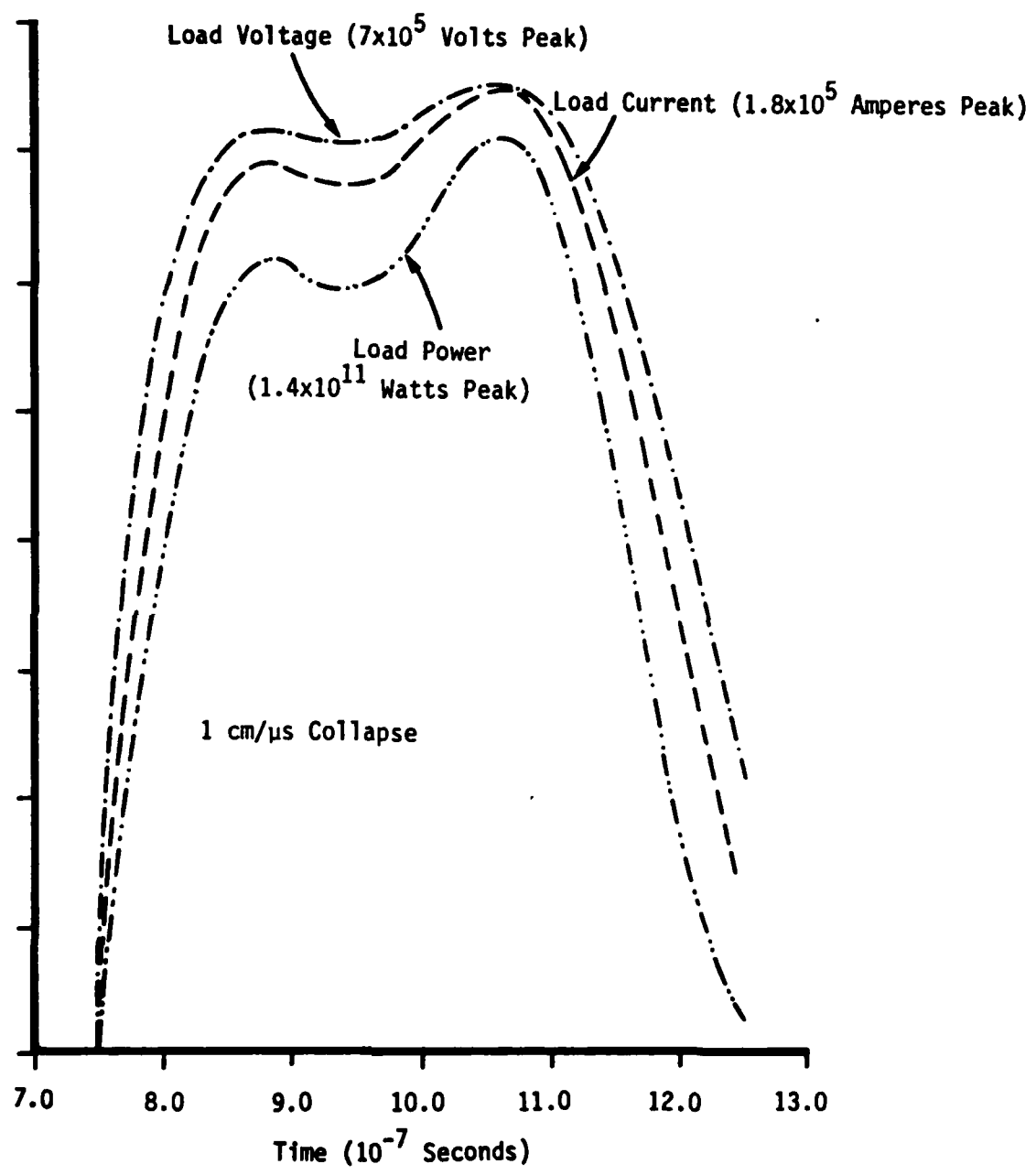


Figure 38. Load parameters for pulse charged lumped element line.

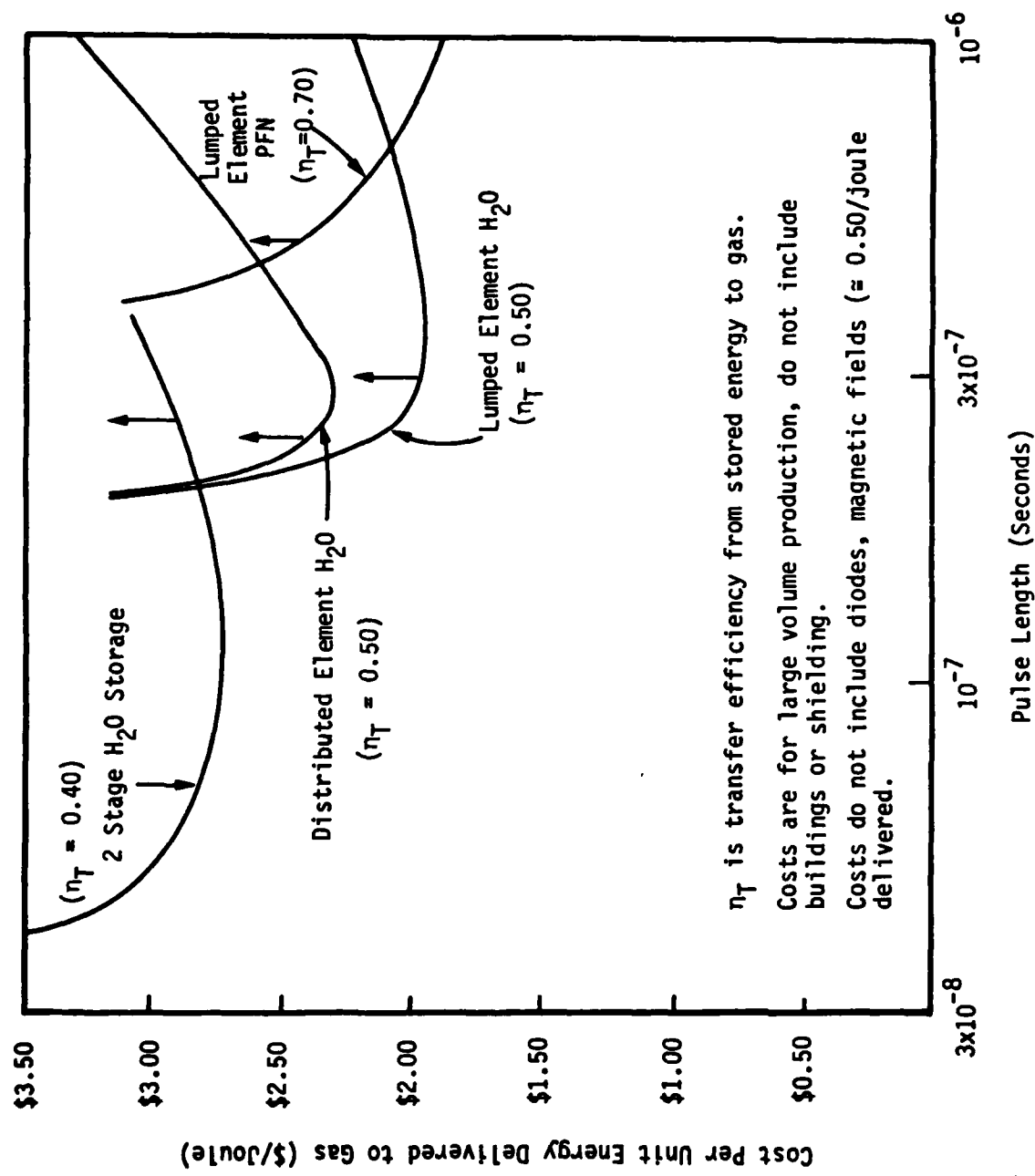


Figure 39. Costs for various types of drivers - large volume production.

electron beam. Field uniformity is particularly important in the vacuum region. The uniformity requirement restricts the types of metals employed structurally, particularly iron. The magnet may be powered either with a DC source or with a pulsed source such as electrolytic capacitors. An energy of $\sim 10^4$ joules is required, and from the standpoint of power supply selection, a DC supply is best.

The field will not be large enough to be troublesome in terms of stresses. Magnet costs for the shorter pulses rise dramatically. The voltage standoff design must be compatible with the B field. A straightforward corona ring shield with anodized aluminum is recommended in the design, with single electrode multiple lead through and an oil transition section.

Summary and Recommendations for Electrical Design

A 400 KV driver with a 2 mil foil and a voltage variation less than $\pm .07$ is envisioned as possible, and represent a reasonable design goal. We recommend a fairly fast metal cased capacitor Marx, with thorough fault condition analysis and multiple vendor capability on component parts. The design should have about 4 multiple lead throughs and a 1 kilogauss side field. Energy storage per side should be about 50 kilojoules and the cathode should be made of felt. Stringent E-beam lint test for reliability should be considered as part of design approval.

Figure 40 shows the energy partitioning in an electrical system, showing a transfer efficiency of 61%. A reasonable goal is 50% transfer efficiency, and with some care in the design 60% may be expected. Higher efficiencies come with greater difficulty, with 70% not unreasonable. An efficiency of 80% should be considered as an upper limit.

In summary, then, the preliminary electrical system specifications include a design goal to deliver 25 KJ per side to the gas in 1 μ sec at a

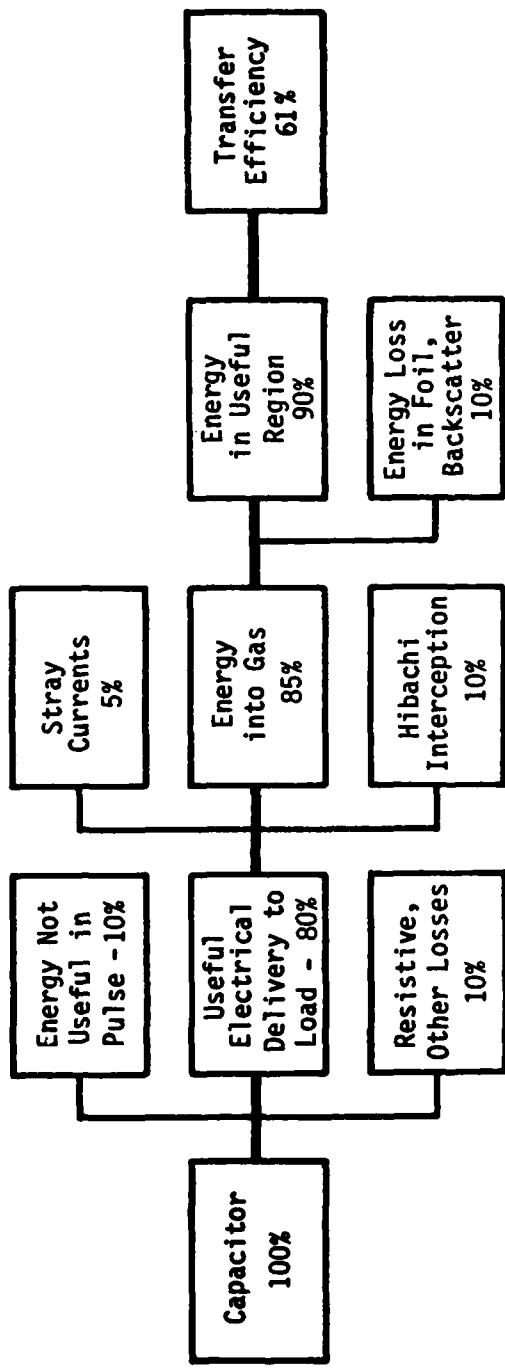


Figure 40. Energy partitioning in electrical system.

transfer efficiency of 60% or more. Delivery of the beam is at a voltage of 400-420 KV, and if a 50% efficiency is assumed, 50 KJ per side must be stored. Less than 1 foil rupture per 200 full shots should be expected, along with a 95% reliability on electricity in a continuing shot sequence. The system will contain the standard timing, control, and safety specifications.

OPTICS AND MOUNTS

The tradeoff of energy extraction between efficiency and sensitivity to absorption and pump changes has been discussed parametrically in a previous section. Kinetic variational information is insufficient to perform a detailed analysis. In this section we will discuss beam quality, coating status, internal and external optics and costs.

To obtain good beam quality, high quality mirrors and windows are required. The former are relatively inexpensive while the latter are more costly. The medium density fluctuations should be low enough to permit diffraction limited operation, and the transient phase shifts should be investigated, since they affect the output uniformity. Finally, a good quality beam will require an unstable resonator. Figure 41 shows the optical geometry for the unstable resonator.

Figure 42 plots the parasitic limit curves for several different cavity dimensions, as defined in Figure 41. For each transverse and longitudinal dimension, the maximum lumped reflectivity is plotted as a function of pump rate for threshold. In addition, the loaded gain is shown, and the range of reflectivities for metals, dielectrics, and AR coatings. At the 2 meter longitudinal scale dimension and loaded gains of $.02 \text{ cm}^{-1}$, a great deal of care must be incorporated into the design to eliminate parasitics, since even AR coatings may reflect enough light to exceed threshold conditions.

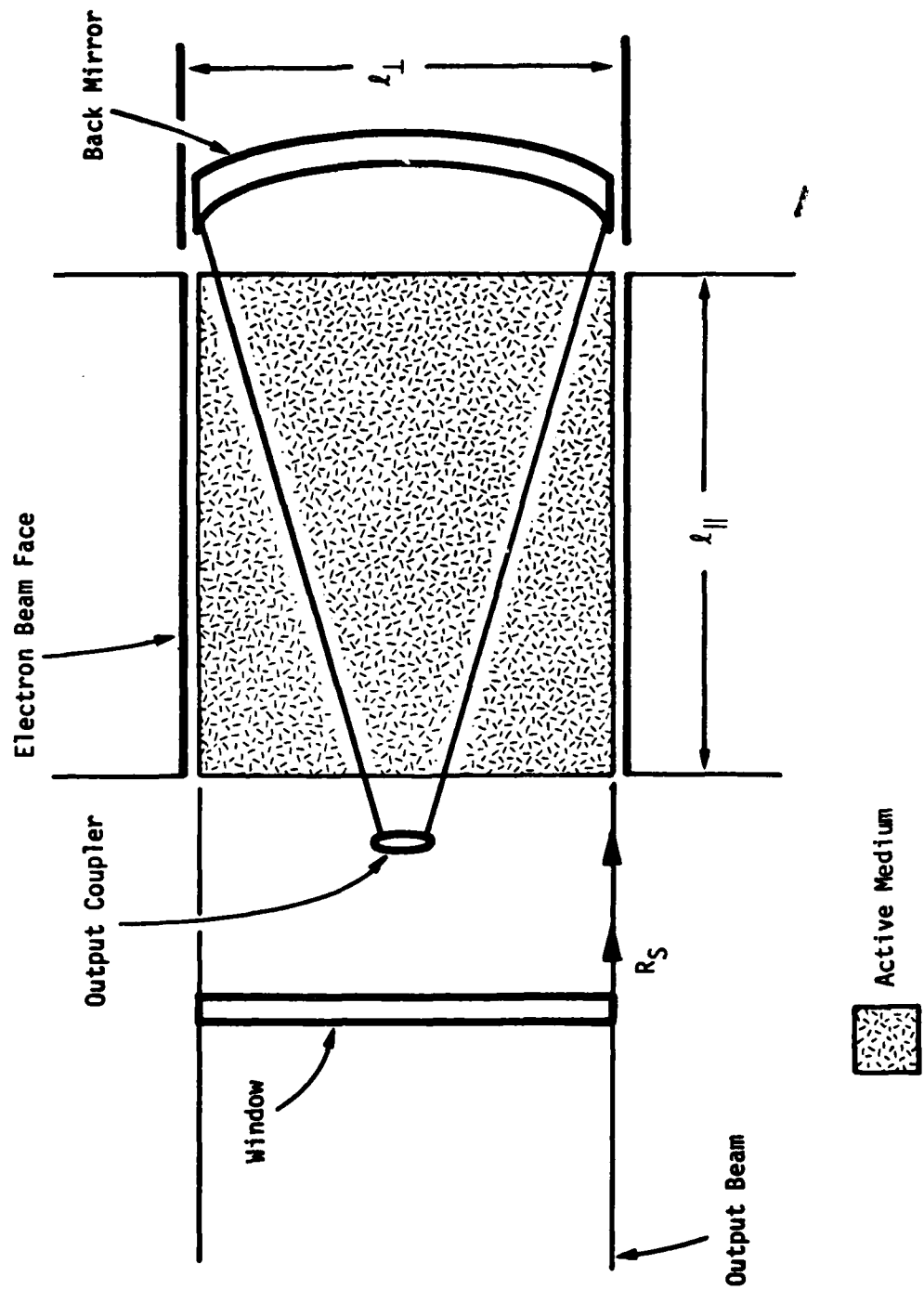


Figure 41. Optical geometry for unstable resonator.

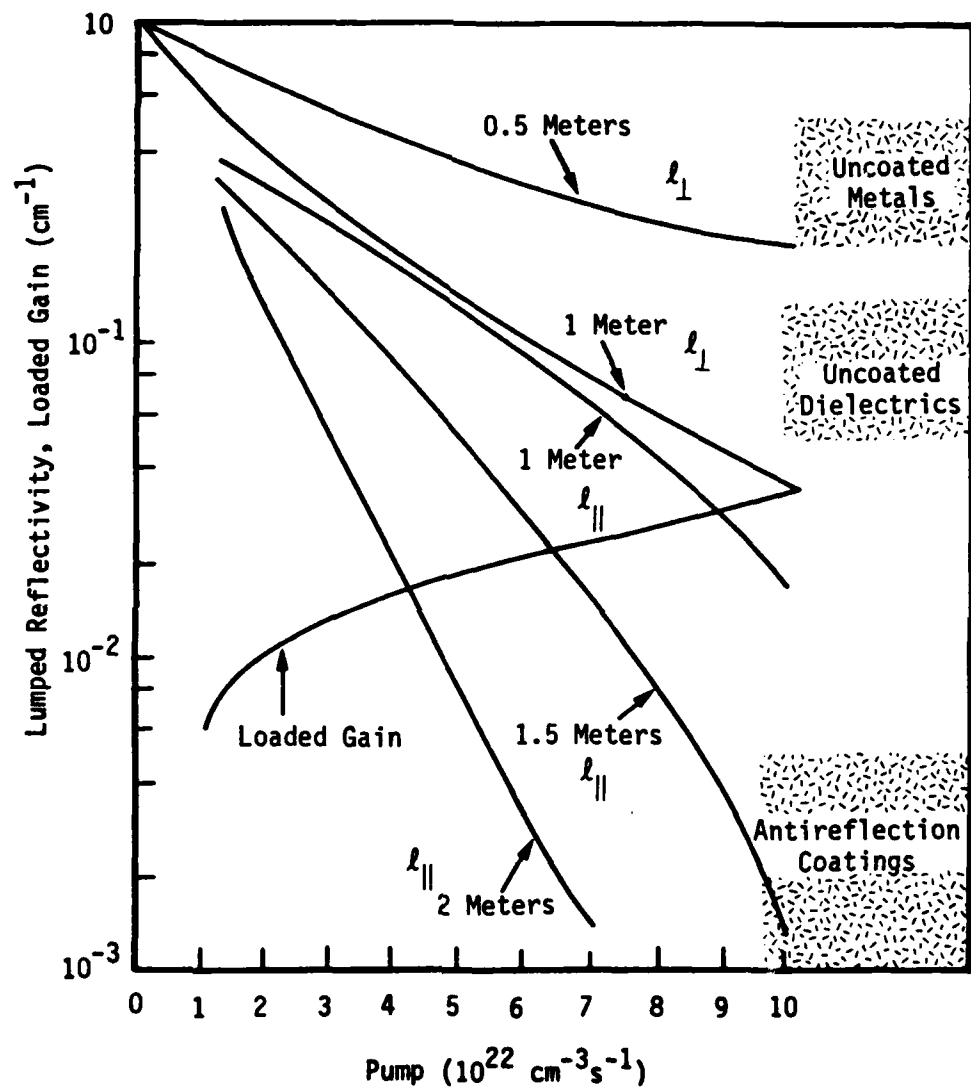


Figure 42. Parasitic limit curves for several different cavity dimensions.

Internally mounted optics tend to give better performance than externally mounted optics, but halogen compatibility of the dielectric coating is essential for the internally mounted mirror. The internally mounted mirrors have lower losses and require less parts than the externally mounted pieces. External mirrors need extra windows and generally require Brewster angle windows.

The unstable resonator is recommended since it is less sensitive to changes in the absorption. Internal mounts are solid pieces and are not very difficult to construct, as long as resolution and stability on the order of 10 microradians are acceptable. The cost should run around \$15 K each.

Table 2 summarizes small lot optics costs for mirrors and windows of both low and good surface quality.

Table 2
Small Lot Optics Costs (1980 Dollars)

	Crude (~ 1λ Pk-Pk)	(λ/10 Pk-Pk)
Mirrors	\$7K/Mirror	\$10K/Mirror
Windows	\$10K ①	\$10K ① + Polishing in transmission (~ \$50K)
	\$15K ②	\$15K ② + Polishing in transmission (~ \$50K)

① Optosil 2 based on 20 inch diameter clear aperture

② Suprasil 2

The coating status with respect to damage is uncertain at present for a 308 nm wavelength, 1 microsecond long pulse with a large spot size. XeF coatings, however, look promising relative to the energy densities required in the present design. As mentioned, halogen compatibility of the coatings is an issue. Energy loadings on the reflective and AR coatings over a 20 inch aperture will be in the $2-4 \text{ J/cm}^2$ range.

In summary, then, we recommend internal mounted optics, a flat resonator for optimum energy output, a near normal incidence AR coated output window and a second unstable resonator set. A damage level in the $2-4 \text{ J/cm}^2$ at 10^{-6} sec and 308 nm is required, with chemical compatibility and damage tests recommended. Output coupling of $\sim 90\%$ is probably a reasonable choice, but the exact value depends on the other medium parameters. Finally, polishing in transmission is required on the large windows for high quality transmission.

OTHER SUBSYSTEMS

The gas handling system design and construction bears heavily on the reliability of device operation, especially in terms of minimizing the probability of a contamination of the chamber. The laser chamber design itself requires several safety and operating considerations, including materials compatibility and operating pressure. Chamber cleanliness and vacuum purity are particularly important when the mirrors are mounted internally. Stainless steel is important if the chamber will be heated, and the metal for the chamber must also be selected based on whether a pulsed or DC magnetic field is used. The method of mechanical alignment to the other elements is important in terms of time spent in checkout and repair. The foil compatibility with Cl_2 is also important.

In addition to these considerations, one must be concerned with radiation shielding, alignment of the windows, all mechanical stresses, and optical and electrical probes and diagnostics.

COST SUMMARY

The cost summary for the system is presented in Table 3, in terms of 1980 Dollars, for both 50 KJ and 25 KJ energy delivery.

Table 3
Cost Summary

Machine Parts

Power Supply	\$500K/\$350K
Vacuum Boxes and Pressure Chamber	70K
Vacuum Systems	30K
Integration Design	70K
Cathode and Bushings	40K
Optics (2 sets, poor beam quality)	50K
Magnetic Field and Structure	150K
Machine Diagnostics, Controls and Shielding	100K
Gas Handling	30K
Miscellaneous	100K
	<hr/>
	1140K/990K

[continued]

(Table 3 continued)

Integration and Checkout Labor, Supplies and Overhead	<u>200K</u>
	1340K/1190K
10% Contingency	<u>134K/ 119K</u>
Subtotal	1474K/1309K
G & A (25%)	<u>369K/ 327K</u>
	1843K/1636K
Fee (10%)	<u>184K/ 164K</u>
Total Cost (1980 Dollars)	2027K/1800K
Inflation for 1.5 Years (x 1.2)	<u>405K/ 360K</u>
Total Project Cost	2432K/2160K

